Supplementary Materials for

Shortwave Emitters Enable Radiative Cooling of Above-ambient Vertical Surfaces

Zhi-Wei Zeng *et al.*

Correspondence author: Xiao Xue and Hai-Bo Zhao, xuexiao-1989@163.com or haibor7@163.com

The PDF file includes:

Materials and Methods

Materials

Boron nitride (BN, 150 nm, 99%) was obtained from Sigma-Aldrich. Thermoplastic polyurethane (TPU, BASF 1185A) was sourced from Kaixuan Plastic Technology Co., Ltd. Titanium dioxide (TiO_2, 300 nm) and 1,1,1,3,3,3-hexafluoroisopropanol were purchased from Aladdin Reagent Co., Ltd. Phosphors including $(Ba,Sr)_2SiO_4:Eu^{2+}$, $Y_3Al_5O_{12}:Ce^{3+}$, and $SrAlSiN_3:Eu^{2+}$ were supplied by Shenzhen Looking Long Technology. Polyformaldehyde (POM) was acquired from DuPont Technology Co., Ltd. Tetrahydrofuran (THF), dimethylacetamide (DMAc), NaOH (Sodium hydroxide), HCl (Hydrochloric acid), and NaCl (Sodium chloride) were purchased from Chengdu Kelong Reagent Co., Ltd. All chemicals were used as received without further purification.

Fabrication of TB

10 g of TPU was added to 90 g of THF and stirred at 50 °C for 4 h until it became clear. Subsequently, BN particles were added to the above solution and continued to be stirred for 4 h until it became a homogeneous suspension. Finally, it was poured into a glass mold and dried at room temperature until THF evaporated completely, and the prepared sample was called TB film. The sample prepared when the BN content is 0 is called transparent or non-porous TPU.

Fabrication of White

10 g of TPU was added to 90 g of THF and stirred at 50 °C for 4 h until it became clear. Subsequently, BN and TiO_2 particles were added to the above solution and continued to be stirred for 4 h until it became a homogeneous suspension. Finally, it was poured into a glass mold and dried at room temperature until THF evaporated completely, and the prepared sample was called White film.

Fabrication of Porous TPU

Firstly, 15 g TPU was added to 85 g Dimethylacetamide (DMAc) and stirred at 50°C for 8 h to form a transparent casting solution. Secondly, the slurry was then scraped onto glass plates. Subsequently, it was placed in a water bath for 12 h. Finally, the samples are dried at 60°C for 48 hours and the sample was called Porous TPU.

Fabrication of Selective

Firstly, 5 g POM was added to 95 g 1,1,1,3,3,3-Hexafluoroisopropanol and stirred at 50°C for 2 h to form a transparent casting solution. Secondly, electrostatic spinning was carried out with a 20-gauge needle tip at an injection rate of 2 ml h^{-1}, a voltage of 18 kV, a distance of 15 cm during spinning, and a relative humidity and temperature of 60% and 25°C. A roller covered with aluminum foil was used to collect the spun filaments. Finally, the samples are dried at 60°C for 48 h and the sample was called Selective.

Characterization

SEM images were taken with a German ZEISS Sigma 300 instrument. The infrared absorbance of the sample was tested using an ATR-FTIR spectrometer (Nicolet 6700). Thermal conductivity was measured using a Hot Disk TPS 2200 instrument. TEM images were taken using a Talos F200S (energy spectrum SUPER X). The refractive index (n) and extinction coefficient (κ) of TPU were measured using an ellipsometer M-2000v and J.A. Woollam RC2. The pore size distribution was obtained using Nano Measurer 1.2. The atmospheric transmittance was simulated by MODTRAN (version 5.0). Infrared photos were taken by infrared thermal imaging devices (FTLR T420). Mechanical tests were performed on an INSTRON 3366 instrument with a sample size of 20 mm*50 mm, and the thickness was 200 μm. Thermal stability was tested with a thermogravimetric analyzer (TG 209F1 Libra) in a nitrogen atmosphere at a heating rate of 10°C/min. Excitation, emission spectra, quantum yields and fluorescence lifetimes were tested using the Edinburgh FLS1000. Chemical resistance was evaluated by immersing the samples in 0.1 M hydrochloric acid, 0.1 M sodium hydroxide, and 0.1 M sodium chloride solutions for seven days, followed by reflectance measurements after drying. Ultraviolet resistance was assessed by exposing the samples to a 365 nm UV lamp for seven days, followed by reflectance measurements to evaluate optical stability. Durability was evaluated by exposing the sample to ambient air for one month, followed by reflectance measurements. Abrasion resistance was tested by manually rubbing the sample back and forth 1,000 times, after which the reflectance was measured to assess any performance degradation.

Supplementary Text

Supplementary Text Note 1: Calculation of theoretical cooling power for horizontal direction.

When an object faces the sky, on the one hand, it radiates electromagnetic waves into the universe, and some of the electromagnetic waves are absorbed by the atmosphere. On the other hand, it absorbs some of the short-wave electromagnetic waves from sun, and is also affected by the convective heat transfer of the surrounding environment (1, 2). According to the law of conservation of energy, theoretical cooling power of an object can be expressed as (3, 4):

$$P_{cool} = P_{rad}(T_m) - P_{atm}(T_{air}) - P_{solar} - P_{non-rad} \quad (1)$$

where T_{air} and T_m are the temperatures of surrounding atmosphere and sample bottom, respectively. $P_{rad}(T_m)$ refers to the radiation power by samples. $P_{rad}(T_m)$ refers to radiation power by samples, and $P_{atm}(T_{air})$ is atmospheric radiation absorbed by material. P_{solar} refers to the solar heat gain absorbed by material. $P_{non-rad}$ refers to the non-radiative heat exchange between the material and surrounding environment, including heat conduction and heat convection. According to Equation 3, necessary condition for P_{cool} to reach its maximum value is maximization of output energy and minimization of absorbed energy. Power emitted by samples can be defined as:

$$P_{rad}\ (T_m)\ = 2\pi \int_0^{\frac{\pi}{2}} sin\,\theta\ cos\,\theta d\theta \int I_{bb}(\lambda, T_m)\varepsilon(\lambda)d\lambda \qquad (2)$$

According to the law of thermal radiation, the part of radiation by an object that is absorbed by atmosphere will eventually return to object in the form of atmospheric counter-radiation, which is specifically expressed as:

$$P_{atm}\ (T_{air}) = 2\pi \int_0^{\frac{\pi}{2}} sin\,\theta\ cos\,\theta d\theta \int I_{bb}(\lambda, T_{air})\varepsilon(\lambda)\varepsilon_{atm}(\lambda, \theta)d\lambda \qquad (3)$$

Among them, atmospheric emittance $\varepsilon_{atm}(\lambda, \theta)$ is specifically defined as:

$$\varepsilon_{atm}(\lambda, \theta) = 1 - \ \tau(\lambda)^{\frac{1}{\cos\theta}} \qquad (4)$$

where, θ is zenith angle, and $\tau(\lambda)$ is the atmospheric transmittance in zenith direction. Both material absorption and transmitted thermal gain will ultimately lead to an increase in temperature of the back surface of sample. Therefore, solar radiative thermal gain on the back surface of material can be defined as:

$$P_{solar} = \int I_{solar}(\lambda)(1 - \rho_{solar}(\lambda))d\lambda \qquad (5)$$

Non-radiative heat transfer power can be defined as:

$$P_{non-rad} = q_{non-rad}\,(T_{air} - T_m) \qquad (6)$$

In non-radiative heat transfer, in order to unify effects of thermal conduction and convection, non-radiative heat transfer coefficient $q_{non-rad}$ is introduced to represent their total effect.

Supplementary Text Note 2: Calculation of theoretical cooling power for vertical direction.

When an object is placed vertically, it receives thermal radiation from the ground and surrounding buildings, in addition to the factors that affect it when facing the sky. According to the law of conservation of energy, the theoretical cooling power of an object can be rewritten as (5):

$$P_{cool} = P_{rad}\ (T_m) - u\ P_{atm}\ (T_{air}) - v\ P_{ground}\ \left(T_{ground}\right) -$$

$$w\ P_{building}\ \left(T_{building}\right) - P_{solar} - P_{non-rad} \qquad (7)$$

u, *v*, and *w* are viewing angle factors, calculated from the fraction of thermal radiation absorbed by the object that comes from the sky, the ground, and the building, respectively (fig. S1) (5, 6).

$$w = \frac{2}{\pi} \int_0^{\gamma} \cos^2\theta_1\, d\theta_1 \int_0^{\alpha} cos\,\theta_2\, d\theta_2 \qquad (8)$$

$$v = 0.5 \qquad (9)$$

$$u = 1 - v - w \qquad (10)$$

where α is the angle between the horizontal plane of the object and the line joining the roof of the building. γ is the angle between the bottom center and the edge of the building (fig. S1). In calculating the cooling power in Fig. 1E and fig. S3, it is assumed to be in an open scenario with only the ground, i.e., γ is 0° and α is 0°.

Power emitted by samples can be defined as:

$$P_{rad}\ (T_m)\ = 2\pi \int_0^{\frac{\pi}{2}} sin\,\theta\ cos\,\theta d\theta \int I_{bb}(\lambda, T_m)\varepsilon(\lambda)d\lambda d\gamma \qquad (11)$$

P_{ground} (T_{ground}) is the power of the ground thermal radiation absorbed by the sample:

$$P_{ground}\left(T_{ground}\right) = 2\pi \int_0^{\frac{\pi}{2}} sin\,\theta\, cos\,\theta d\theta \int I_{bb}(\lambda, T_{ground})\varepsilon(\lambda)\varepsilon_{ground}(\lambda)d\lambda d\gamma \quad (12)$$

The spectral emissivity of the ground is typically ε_{ground} = 0.9 (7).

Supplementary Text Note 3: Finite difference times domain simulation.

We simulated the optical scattering of materials using Lumerical (Finite difference time domain) FDTD software. Lorentz-Mie theory is an exact solution to Maxwell's boundary conditions, which can reflect interaction between particles and light of similar wavelengths. In our calculations, we consider BN as cylinders and spherical particles as solid spheres, both injected into thermoplastic polyurethanes with no porous structure. The diameter of the spherical particles is set to 400 nm. BN is a cylinder where the diameter of the circle is 400 nm and the thickness is 50 nm. The refractive index of BN and spherical particles were defined as 2.131. The refractive index of thermoplastic polyurethane was set to 1.5. The simulated wavelength is set to 500 nm at the strongest point of solar radiation. It is total-field scattering field (TFSF) and scattering efficiency after the division of the perfectly matched layer (PML) boundary condition.

Supplementary Text Note 4: Calculation method for samples reflectance and emittance.

Reflectance and emittance are the most important parts to express performance of radiant cooling. Reflectance can resist the heat gain caused by solar radiation, which can be expressed as:

$$\bar{\rho}_{solar} = \frac{\int I_{solar}(\lambda)\rho_{solar}(\lambda)d\lambda}{\int I_{solar}d\lambda} \quad (13)$$

where λ refers to wavelength, I_{solar} refers to the solar irradiance at 48°N, and ρ_{solar} refers to the reflectance of the samples at a certain wavelength. And emittance can radiate energy of object surface in form of electromagnetic waves into universe, which can be expressed as:

$$\bar{\varepsilon}_{MIR} = \frac{\int I_{bb}(\lambda,T)\varepsilon_{MIR}(\lambda)d\lambda}{\int I_{bb}(\lambda,T)d\lambda} \quad (14)$$

where ε_{MIR} refers to emittance of samples at a certain wavelength. According to Kirchhoff's law of thermal radiation, an object absorbs and emits equal amounts of heat in a state of thermal equilibrium, so emittance is defined as: $\varepsilon(\lambda) = 1 - \rho - \tau$.

Planck introduced concept of quantum, clarified discontinuity of energy, and proposed the relationship between wavelength and radiation intensity based on this, namely:

$$I_{bb} = \frac{c_1}{\lambda^5}\frac{1}{\frac{c_2}{e^{\lambda T}-1}} \quad (15)$$

where C_1 is Planck's first constant, C_2 is Planck's second constant, and T refers to temperature (assumed to be 300 K).

Supplementary Text Note 5: Calculation of color characteristics.

The color characteristics of the photoluminescent particles and TBCs were calculated from their reflectance spectra and the spectral intensity of the D65 light, and the observer's angle is 2° (For more information, see https://www.qtccolor.com/secaiku/tool/convert?m=yxy). Spectral-to-color conversion was performed using the CIE1931 model. Using the spectral reflectance intensity and the color matching function, the parameters x, y, L, C, and h corresponding to the coordinates in the CIE1931 color space can be calculated.

Supplementary Text Note 6: Calculation of effective reflectance of TBC.

For all non-fluorescent samples, the effective reflectance (ER) is equal to the directly measured solar reflectance. Fluorescent samples, on the other hand, do not have a direct measurement of reflectance in their activated state due to photoluminescence. In the actual testing process, ER always shows a certain relationship with the temperature. In order to better quantify the contribution of photoluminescence, we fit the relationship between ER and temperature as (8-10):

$$T = a * ER + b \tag{16}$$

where a and b are real-time parameters fitted to the reflectance and temperature of the TB film and White film.

Supplementary Text Note 7: Calculation of photo conversion efficiency.

When photon wavelengths are converted downward, the photon conversion efficiency is the ratio of the total energy of the photons emitted at the emitted wavelength to the total energy of the photons absorbed. The theoretical photon conversion efficiency $\varepsilon(\lambda)$ depends on the emission and absorption wavelengths and is calculated as (11):

$$\varepsilon(\lambda) = \frac{E_{em}}{E_{ab}} = \frac{\left(\frac{hc}{\lambda_{em}}\right)}{\left(\frac{hc}{\lambda_{ab}}\right)}\phi(\lambda) = \frac{\lambda_{ab}}{\lambda_{em}}\phi(\lambda) \tag{17}$$

where h is Planck's constant, c is the speed of light in vacuum, $\phi(\lambda)$ is the quantum yield of the photoluminescent particles, and λ_{ab} and λ_{em} are the absorption and emission wavelengths, respectively.

Supplementary Text Note 8: COMSOL temperature simulation.

Temperature simulations of TBC, selective and piping were carried out using COMSOL Multiphysics 6.2 software. The material is a typical cylindrical pipe (300 cm · π · 30^2 cm) with a wall thickness of 0.2 cm. The heated copper core has the same dimensions as the material, a thickness of 1 cm, and is connected directly to the inner wall of the pipe. The simulated temperature refers to the temperature at the center of the internal heating element, which is consistent with the actual test conditions. The thermal conductivity of the pipe was set to 16 W m^{-1} K^{-1}. To eliminate the influence of interfacial thermal resistance in the simulation, the thermal conductivity of both the selective and TBC layers was uniformly assigned a value of 0.753 W m^{-1} K^{-1}, with a fixed thickness of 200 μm. In the coordinate system used, the X-axis corresponds to the northward direction, Y to west, and Z aligns with solar incidence. Optical properties of the materials, solar irradiance, and ambient temperature were all derived from experimental

measurements. The simulation model, depicted in Fig. S46, replicates the geometry and structure of the experimental pipe, scaled proportionally. Heat generated by the internal heating element is transferred to the pipe wall and then conducted into the TBC layer. The TBC is subjected to three primary thermal processes: conduction from the pipe, radiative exchange with the environment, and convective heat transfer (12).

1. The TBC surface is subjected to a solar heat flux of 700 W m^{-2}, while simultaneously radiating thermal energy to outer space, the atmosphere, the ground, and surrounding structures. This radiative exchange is calculated based on experimentally determined optical properties of the TBC.
2. Convective heat transfer is incorporated using a natural convection model representative of light wind conditions (class 2).
3. The TBC receives conductive heat from the underlying pipe structure, which is heated directly by embedded heating elements.

Supplementary Text Note 9: Energy-saving simulation.

Energy savings across different climate zones were simulated using the OpenStudio application (version 1.1.7) in conjunction with EnergyPlus (version 23.2.0). Representative meteorological data from central cities within each Köppen climate classification zone were used to assess the regional performance of the cooling strategy. Simulations were conducted using the default equipment room model provided within the software framework. The internal heat load was set to 500 W m^{-2}. Only the thermal and optical properties of the exterior walls and roof were modified to reflect the characteristics of the TBC, while all other parameters were retained as default. Meteorological data were from the official website of EnergyPlus. The total area of the equipment room was 9 square meters. In order to better characterize the impact of the heating equipment, we assume that the equipment room is made of stainless steel sheets (SSS). The energy saving potential of TBC was compared to that of the original SSS equipment room (emissivity 0.125, solar reflectivity 0.678, thermal conductivity 16 W m^{-1} K^{-1}). An indoor HVAC system was incorporated into the simulation to maintain operational stability. Cooling was activated when the indoor temperature exceeded 50 °C, and energy savings were quantified by comparing the total cooling energy consumption with and without the TBC implementation.

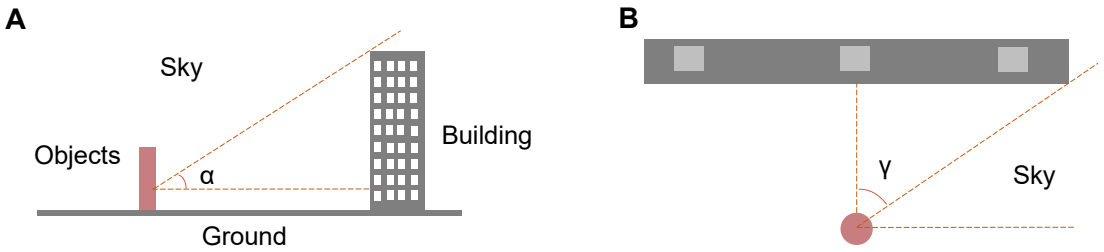

Fig S1. Schematic diagram of a vertically oriented object for radiative cooling. (A) Schematic of a side view of the building angle (α) between the ground and the line connecting the object to the building apex. (C) Top view schematic showing the angle γ between the bottom center and bottom side of the building.

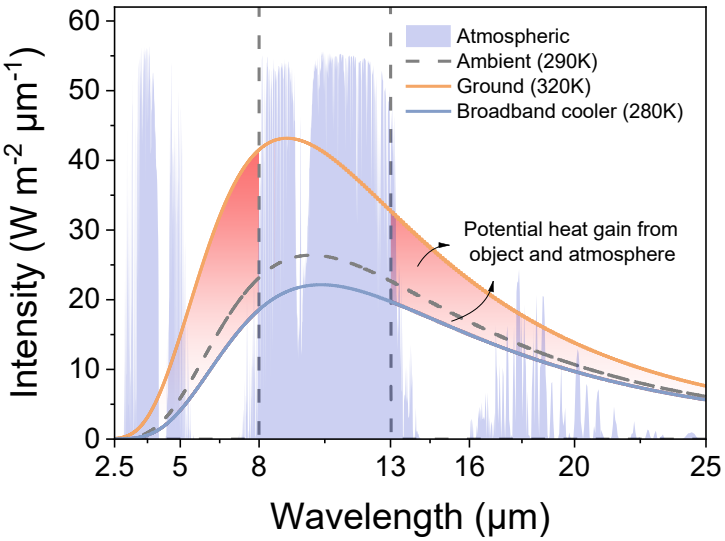

Fig S2. Spectral distribution of radiation intensity. Broadband cooler can obtain additional heat sources (atmosphere, ground and surrounding objects) from non-atmospheric window bands.

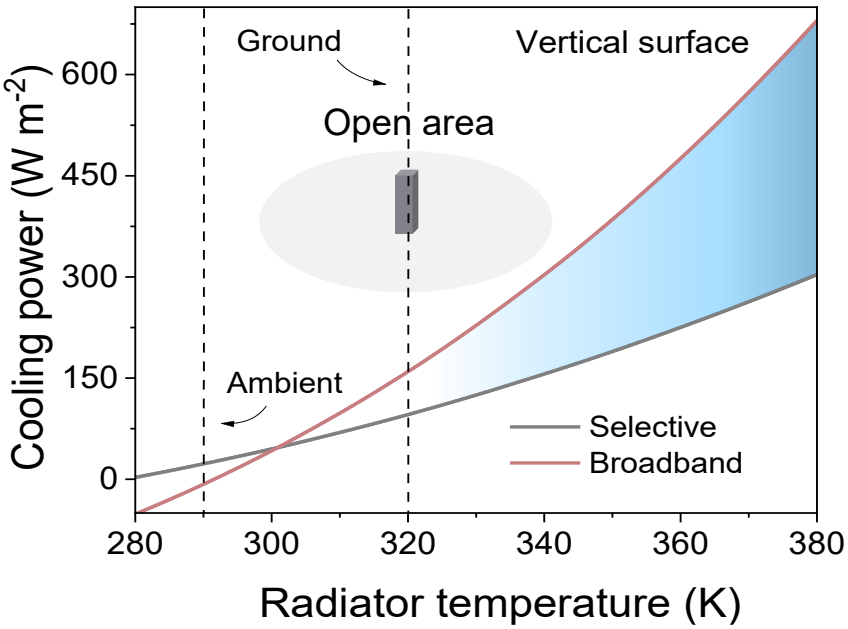

Fig S3. Cooling power of the selective and broadband coolers placed vertically in an open scenario. At elevated ground temperatures and in the absence of internal heat generation, the cooling power of the broadband cooler surpasses that of the selective cooler once the sample temperature exceeds ambient by approximately 11°C.

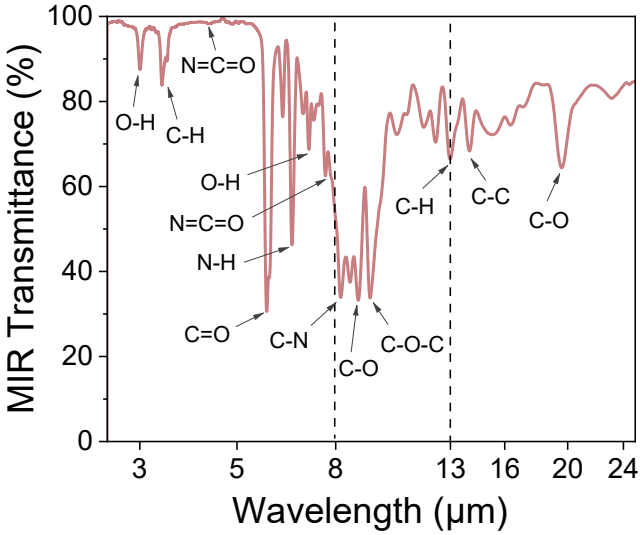

Fig S4. FTIR spectrum of TPU. Its absorption peaks are broadly distributed across the mid-infrared region. Pronounced absorption within ATW arises from C-O-C and C-O groups, which introduce multiple vibrational modes along the molecular chain. Additional functional groups, including N-H, O-H, N=C=O, and C=O, contribute to absorption in the shortwave infrared, while C-C bonds and backbone vibrations further enhance absorption across the broader MIR spectrum (13-15).

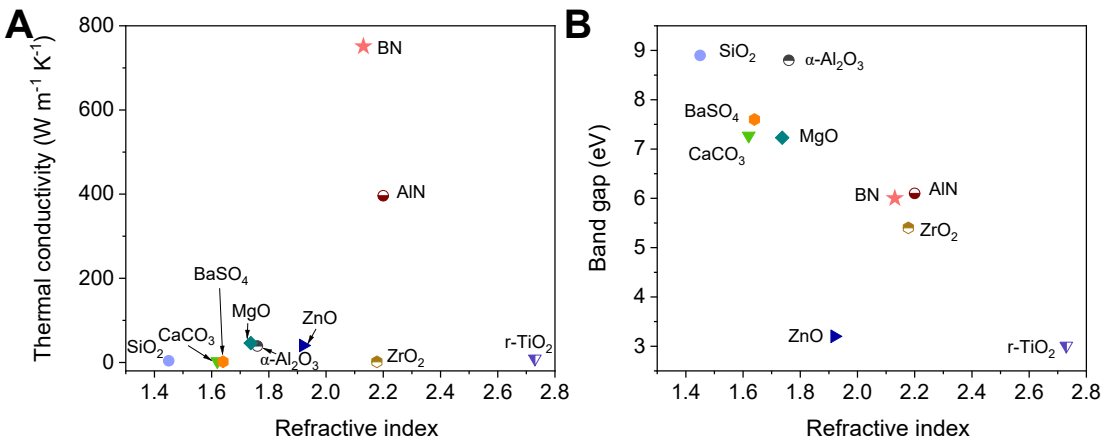

Fig S5. Thermal conductivity (A) and band gap (B) versus refractive index for commonly used dielectric particles with high refractive index or high thermal conductivity. Reference: SiO_2 *(16-18)*, α-Al_2O_3 *(19-21)*, $CaCO_3$ *(22, 23)*, BN *(24-26)*, AlN *(27-29)*, ZnO *(30-32)*, TiO_2 *(33-35)*, ZrO_2 *(36-38)*, $BaSO_4$ *(39-41)*, MgO *(42-44)*.

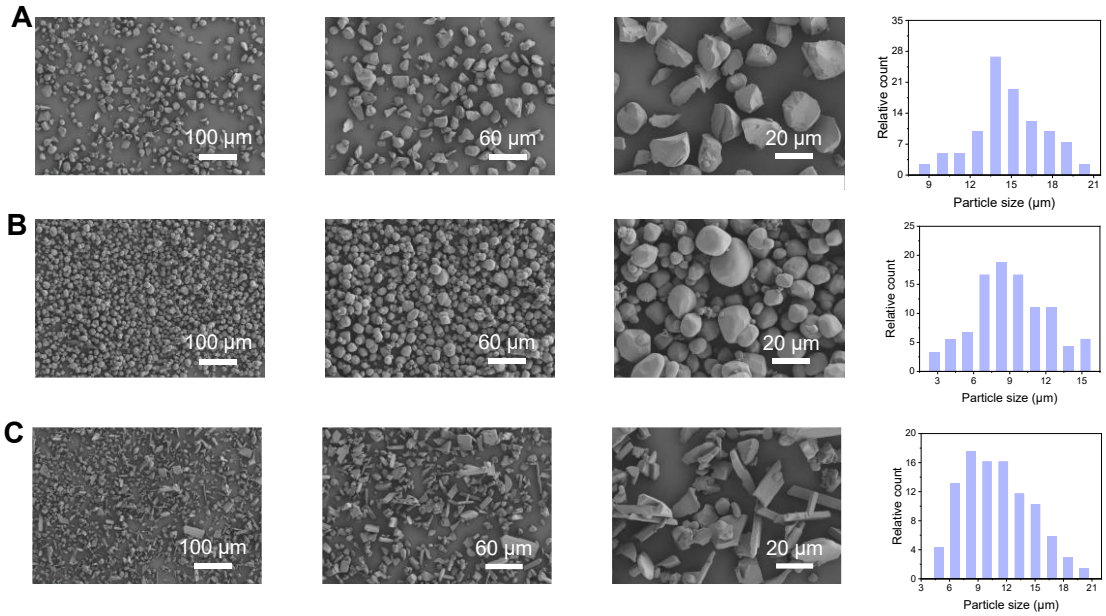

Fig S6. SEM images of (A) green, (B) yellow and (C) red photoluminescent powders at different magnifications and their respective particle size distributions where the average particle sizes of green, yellow and red photoluminescent powders are 14.8 μm, 9.1 μm and 11 μm, respectively.

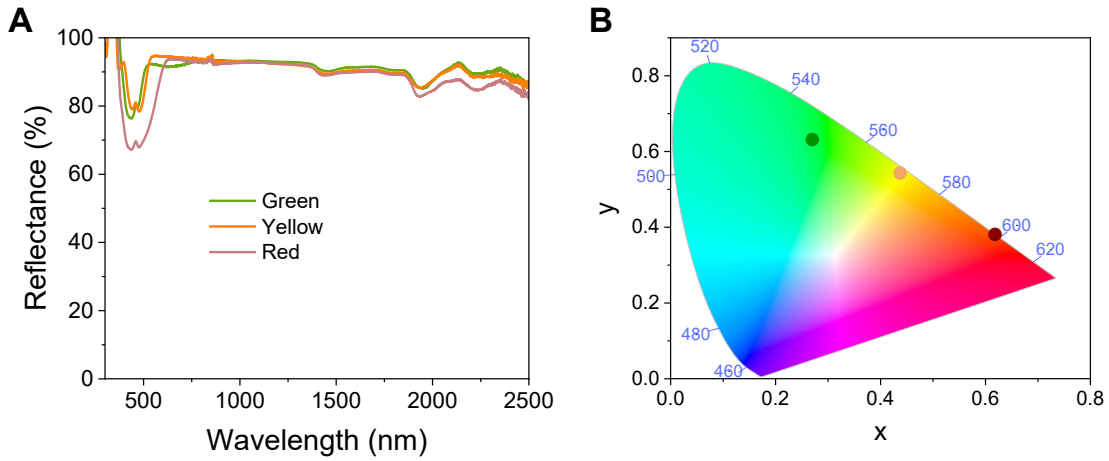

Fig S7. (A) Solar reflectance patterns of green, yellow, and red photoluminescent powders. (B) Chromaticity of green, yellow and red photoluminescent powders shown in CIE 1931 color space.

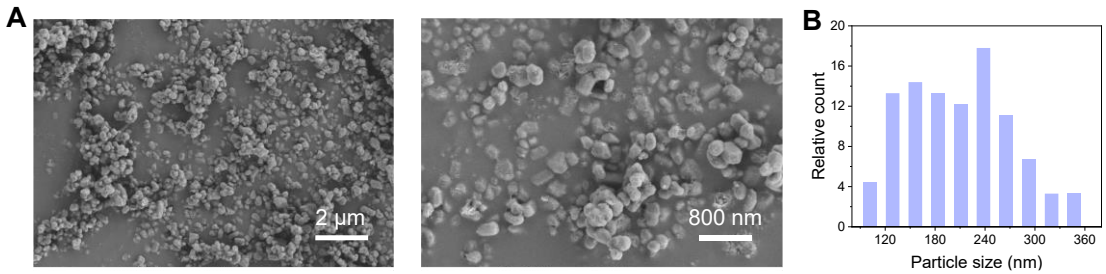

Fig S8. (A) SEM images of titanium dioxide at different magnifications and (B) its particle size distribution with an average particle size of 209 nm.

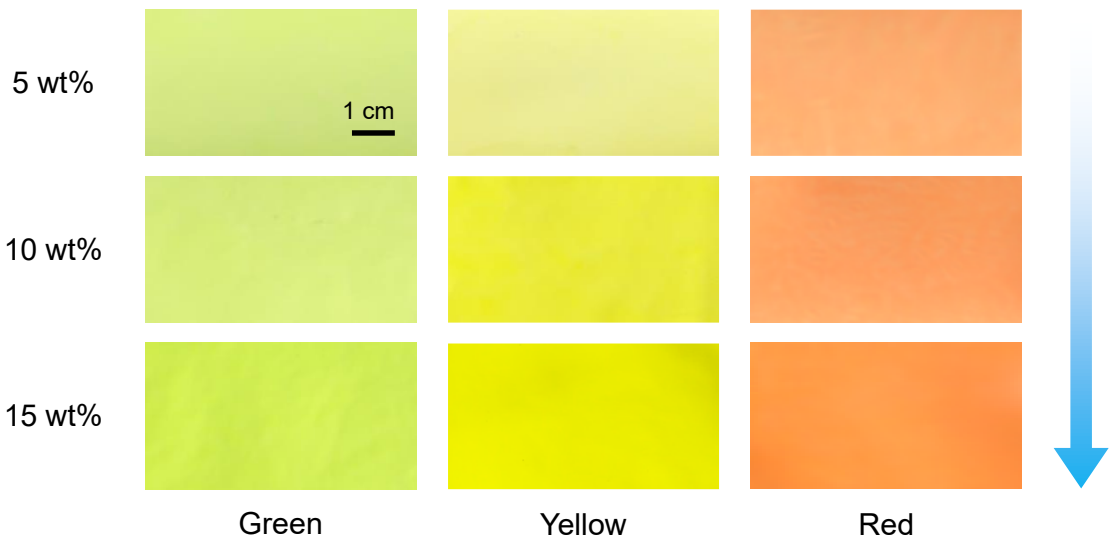

Fig S9. Photographs of TBC prepared by doping different colors of photoluminescent particles.

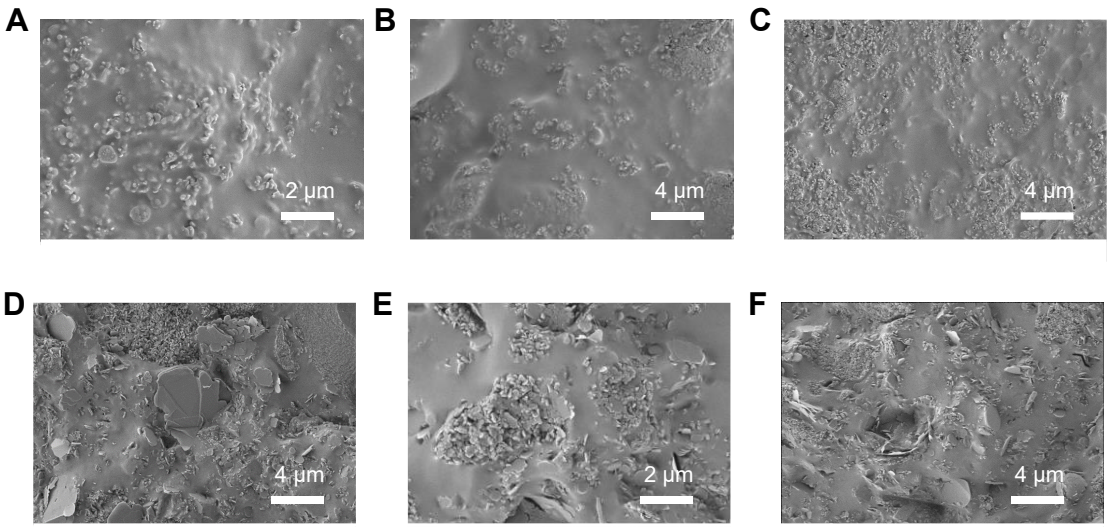

Fig S10. SEM images of (A) green, (B) yellow and (C) red TBC surfaces, and (D) green, (E) yellow and (F) red TBC cross sections.

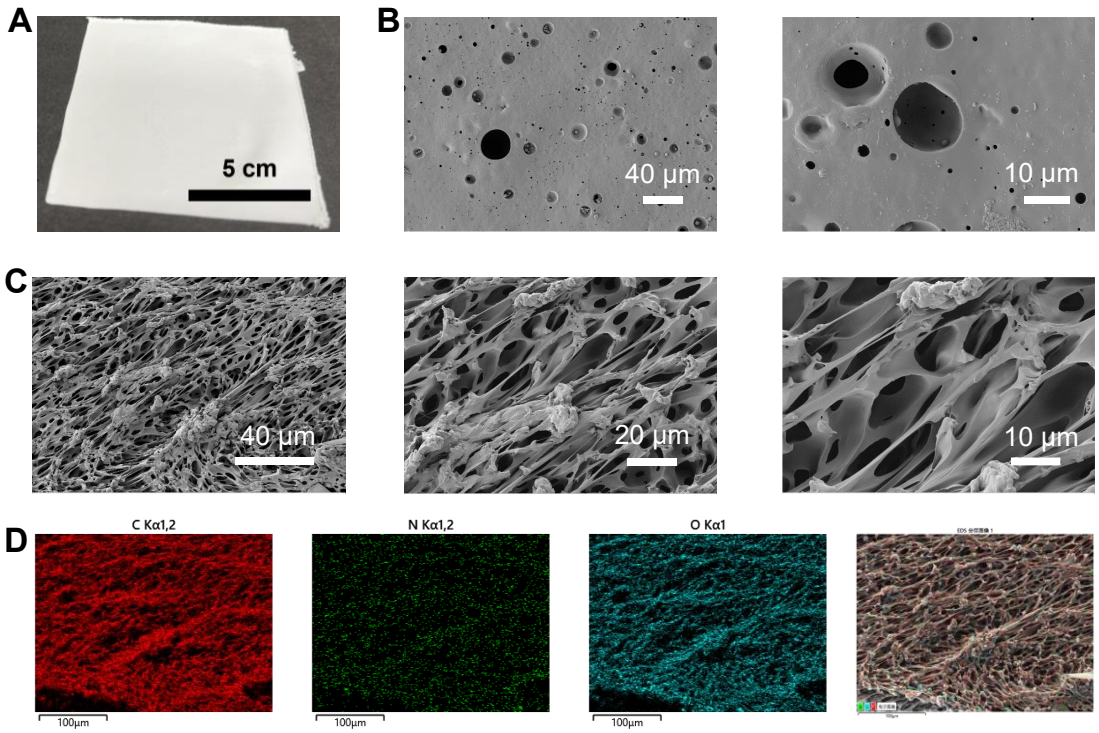

Fig S11. (A) White color appearance of porous TPU. Surface (B) and cross section (C) SEM of porous TPU with large number of porous structures and (D) its elemental distribution.

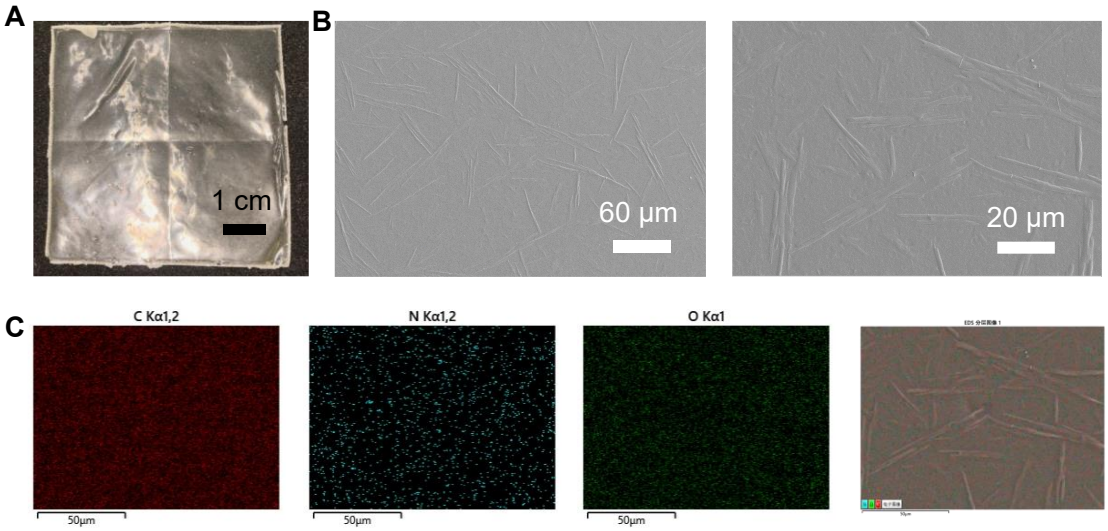

Fig S12. (A) Transparent appearance of non-porous TPU. (B) SEM of the surface of non-porous TPU at different magnifications. (C) Elemental distribution.

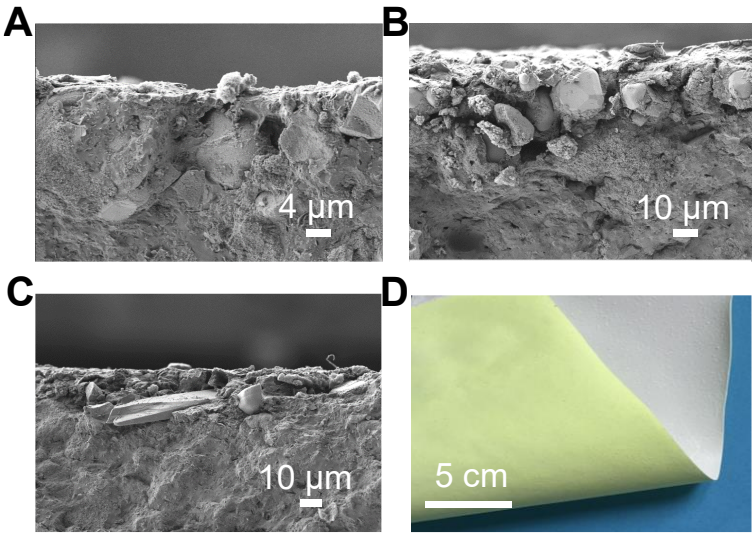

Fig S13. (A) SEM cross-sectional images of the top layer of (A) green, (B) yellow, and (C) red TBC films. (D) Photo of both sides of the TBC film.

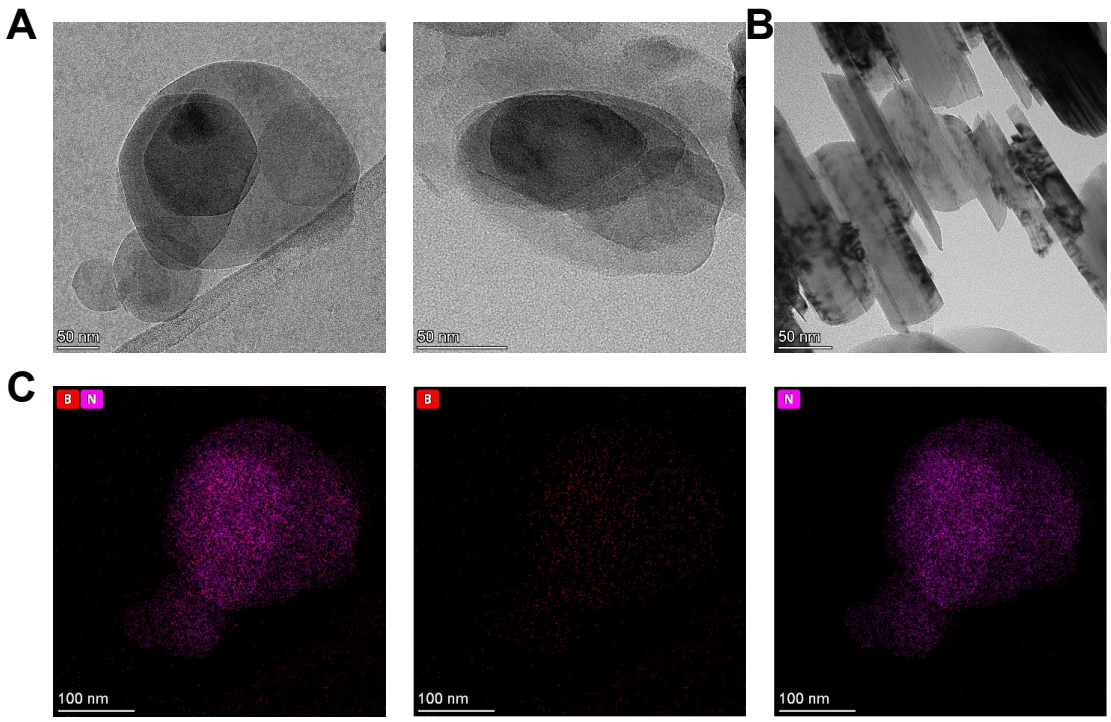

Fig S14. TEM image of BN: (A) surface and (B) cross-section. (C) Elemental distribution.

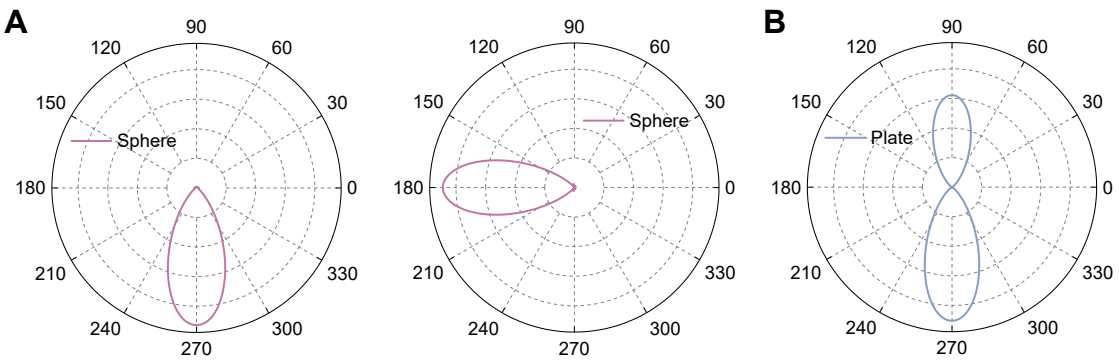

Fig S15. Polarization diagrams of spherical particles in different directions (A) and BN (B) with 0.5-μm wavelength illumination.

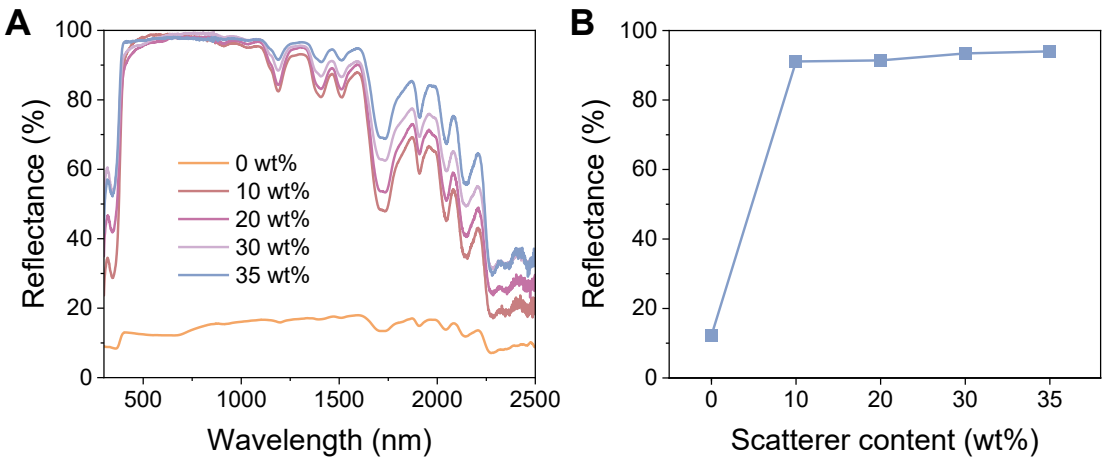

Fig S16. Solar reflectance curves (A) and their reflectance (B) for TB samples with different BN contents.

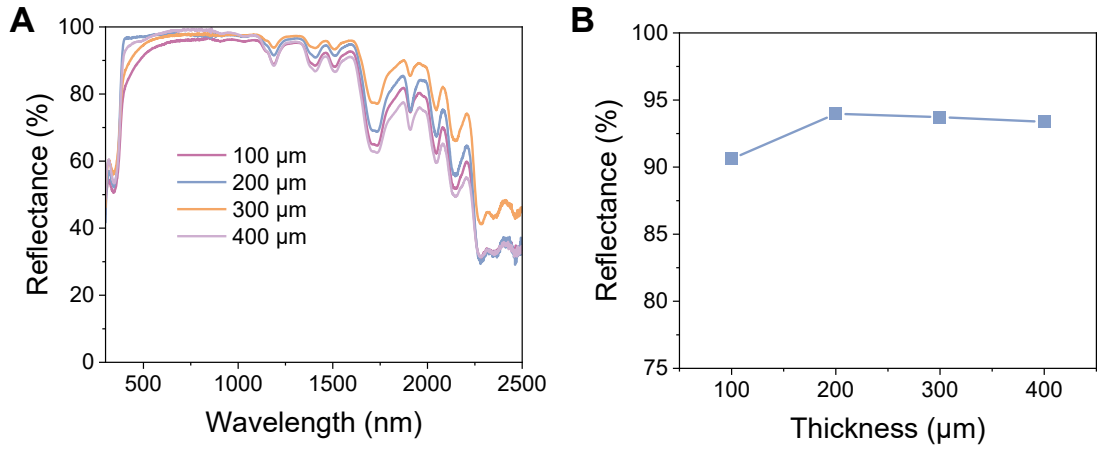

Fig S17. Solar reflectance curves (A) and their reflectance (B) for TB samples with different thicknesses.

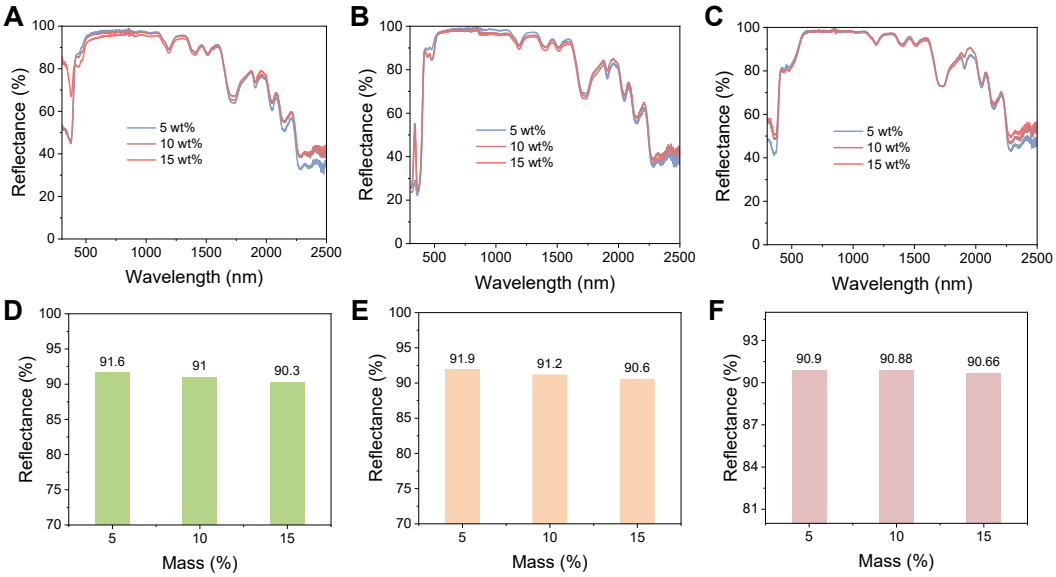

Fig S18. Solar reflectance curves of different concentrations of (A) green TBC, (B) yellow TBC and (C) red TBC and (D-F) their respective reflectance.

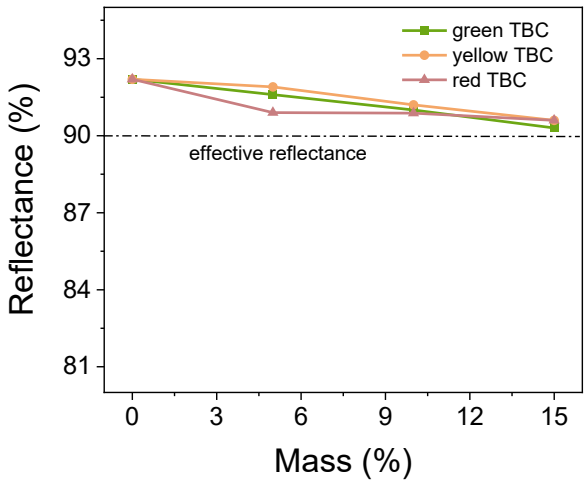

Fig S19. Solar reflectance of different concentrations of green, yellow and red TBC.

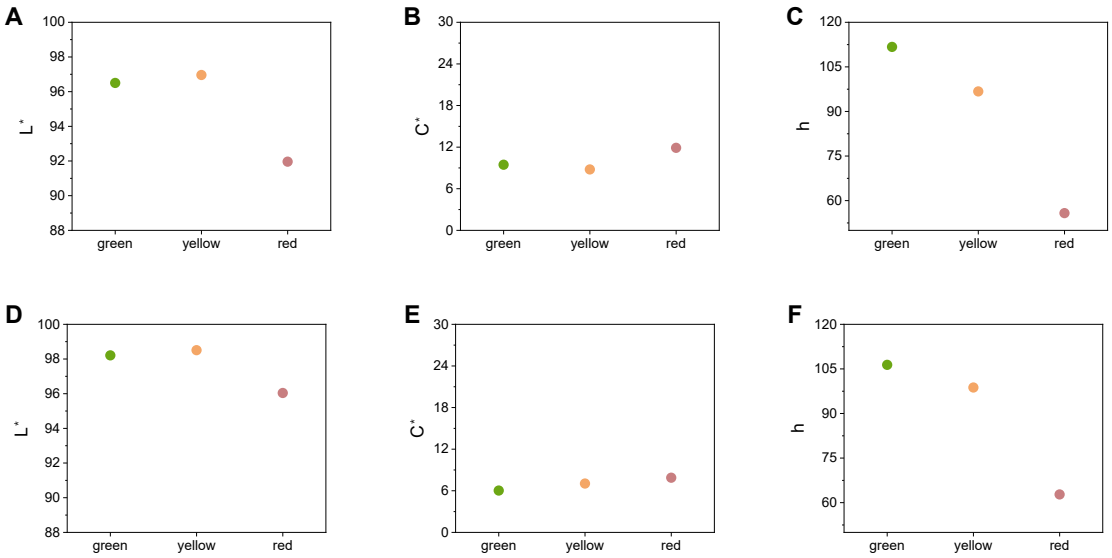

Fig S20. L* (A), c* (B), and h (C) values for colored photoluminescent particles, and (D) L*, (E) c*, and (F) h values for colored TBC. The sub-ambient cooling is considered effective when the value of L is greater than 88 or when the value of c is less than 30 (45, 46).

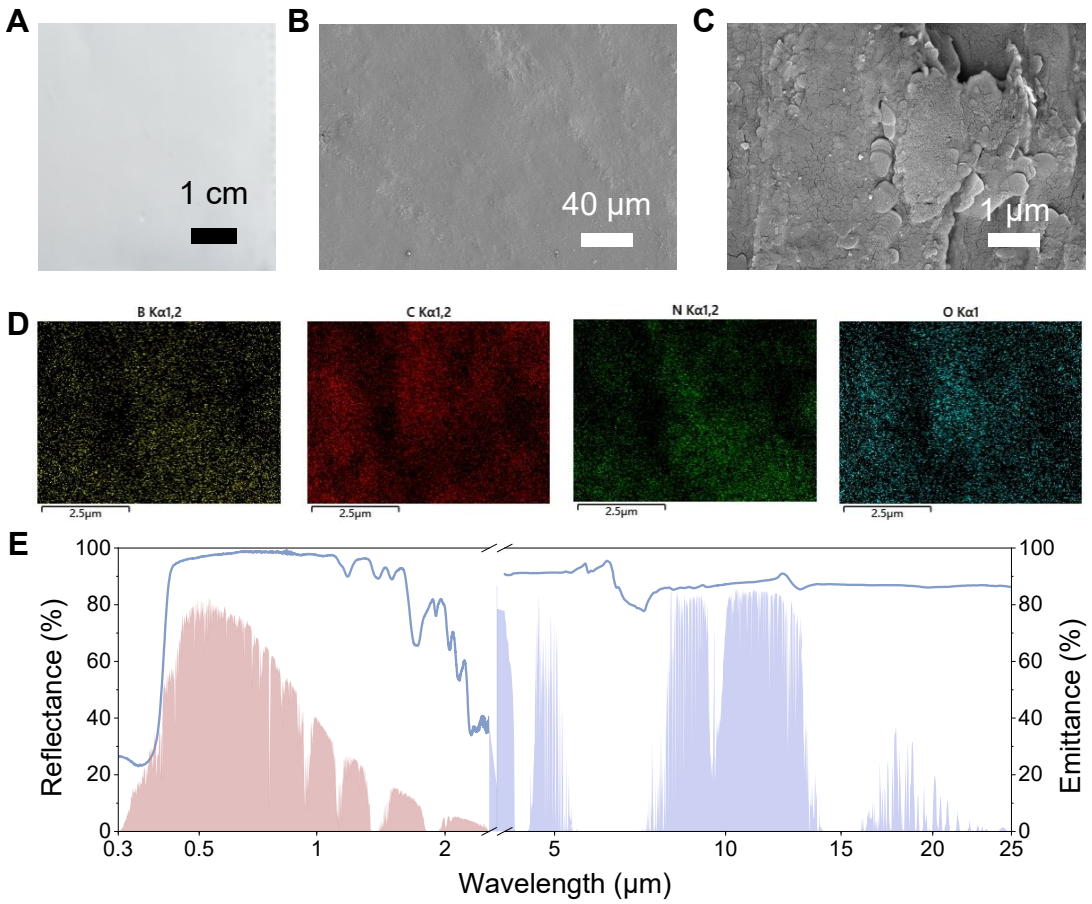

Fig S21. (A) White color appearance of TB film. Surface (B) and cross section (C) SEM of TB film. (D) Elemental distribution. (E) Reflectance and emissivity of a 200-μm-thick White film.

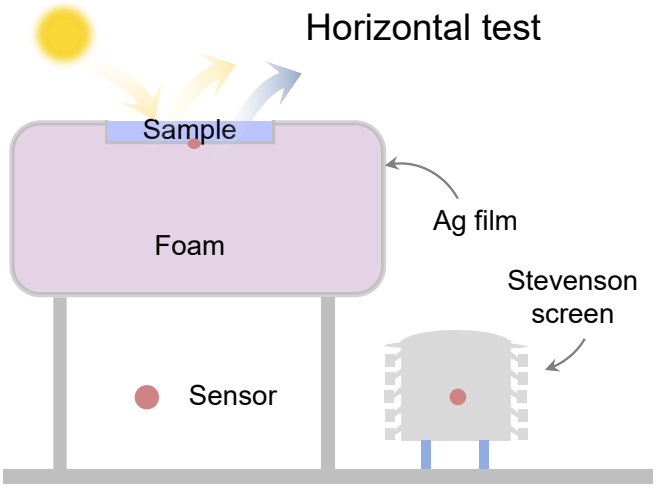

Fig S22. Schematic of the device in the horizontal direction at room temperature.

Fig S23. Outdoor test photos of TBC when placed horizontally at room temperature. Ambient temperatures were tested using a Stevenson screen.

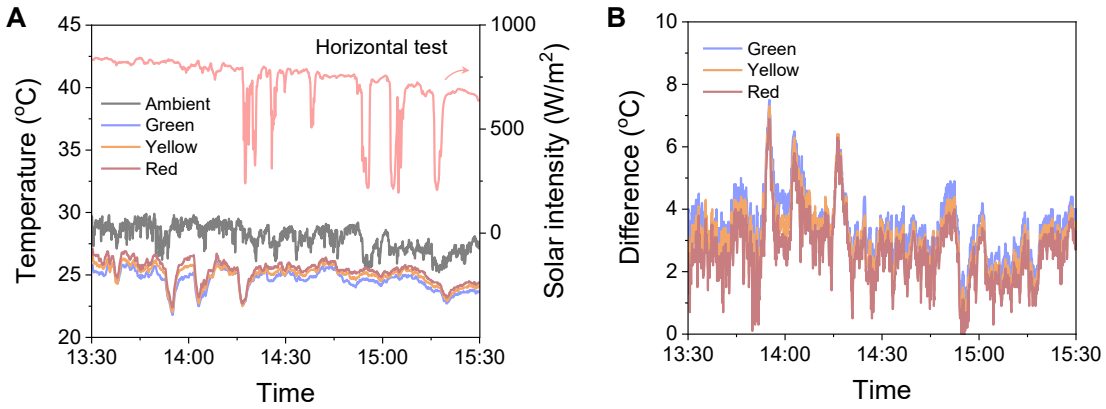

Fig S24. Real-time temperature curves (A) and their difference with ambient temperature (B) of various TBC under direct sunlight when placed horizontally (Chengdu, October 22, 2024).

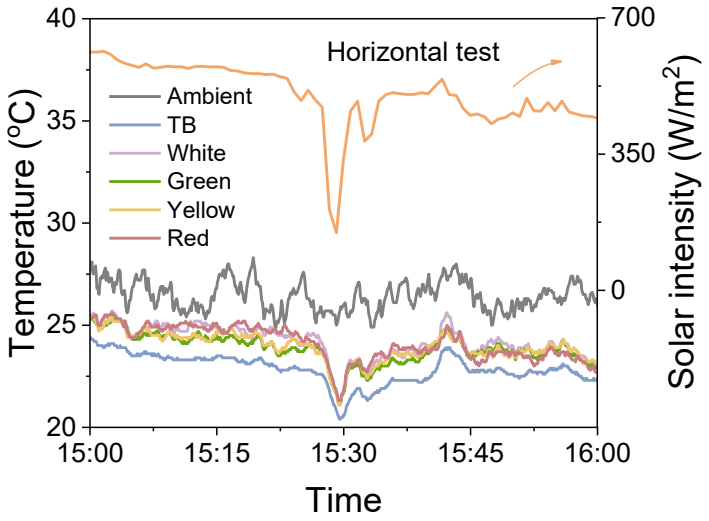

Fig S25. Real-time temperature curves of various samples under direct sunlight when placed horizontally (Chengdu, October 27, 2024).

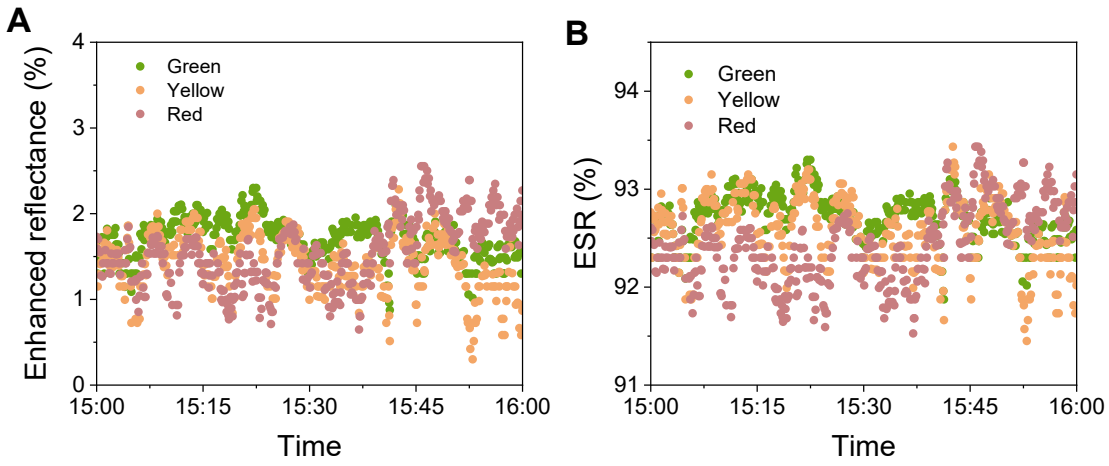

Fig S26. Enhanced reflectance (A) and ESR (B) calculations for various TBC samples corresponding to the TB and White films.

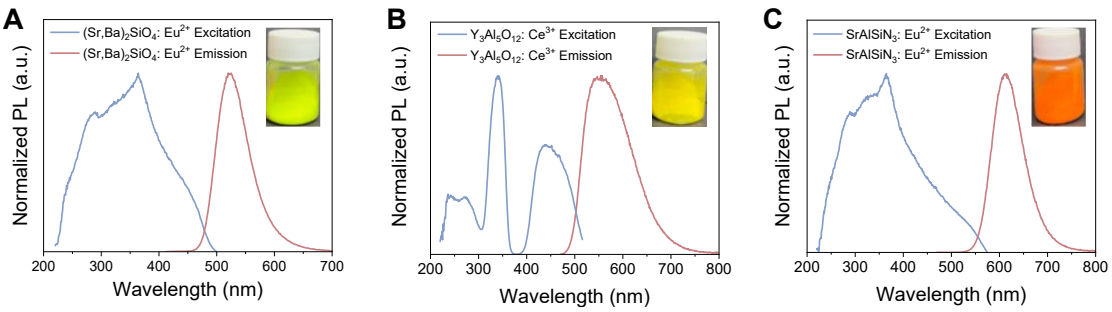

Fig S27. Normalized excitation and emission spectra of a green phosphor (A), a yellow phosphor (B), and a red phosphor (C). Insets are the corresponding optical images of these phosphors.

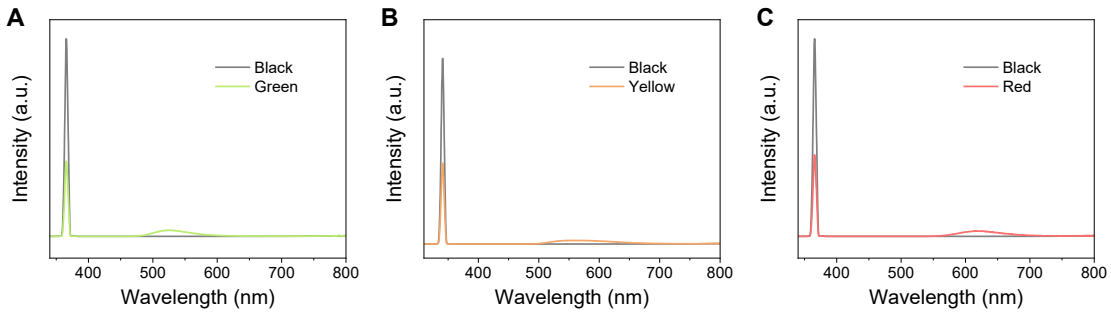

Fig S28. PL emission spectra of blank (without sample, black line) and the (A) green (green line), (B) yellow (yellow line) and (C) red (red line) used for measuring the photoluminescence internal quantum yields.

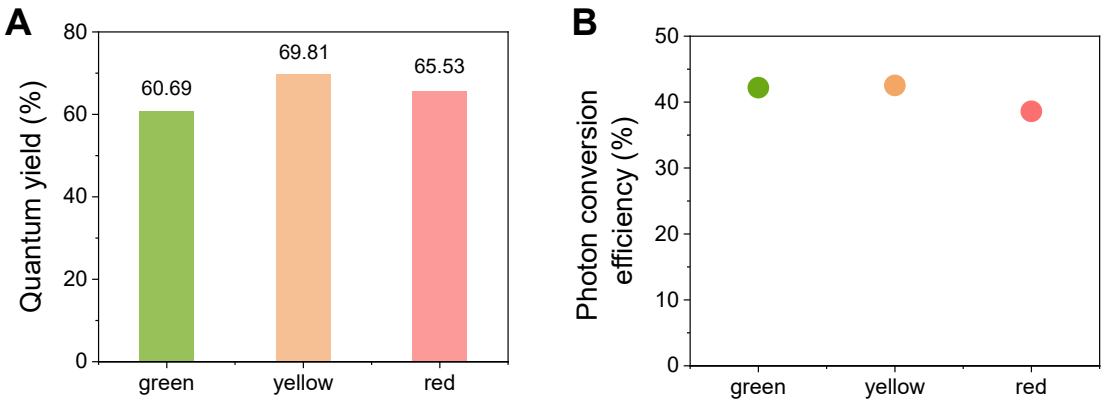

Fig S29. Quantum yields (A) of three photoluminescent particles, and (B) their photonic conversion efficiencies.

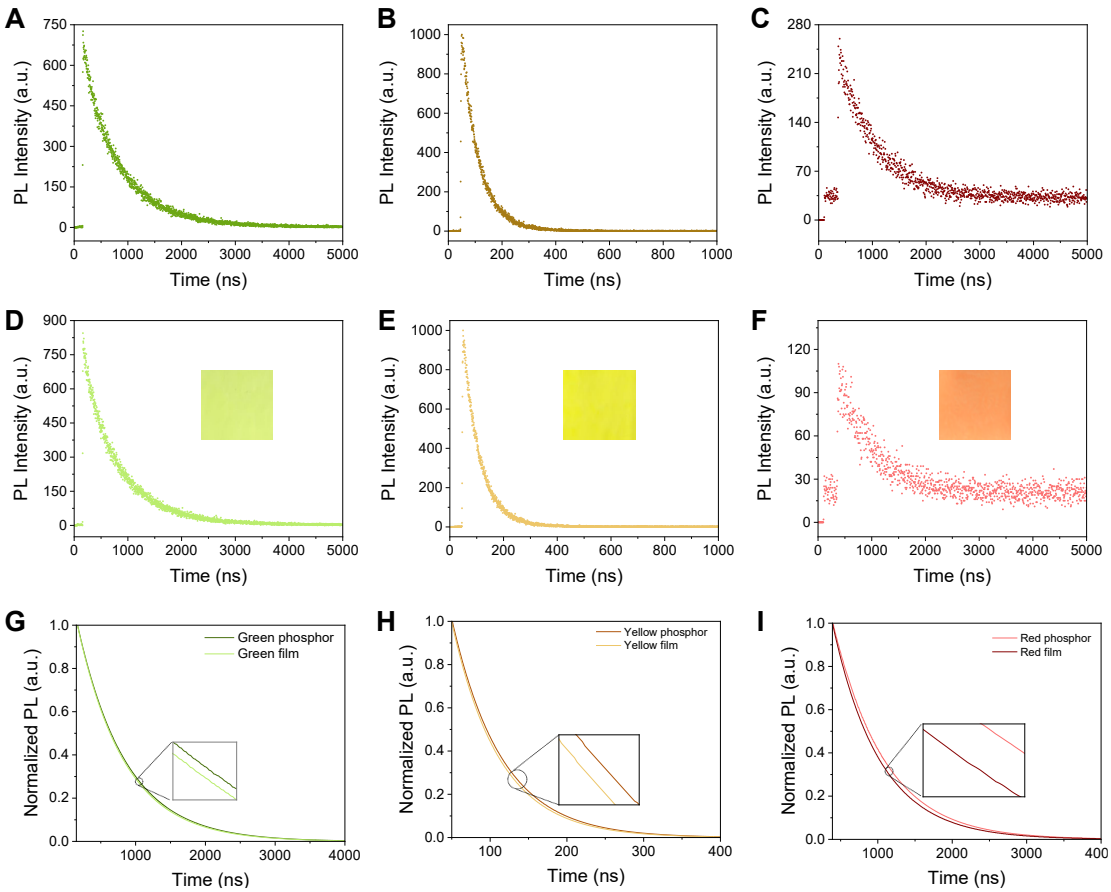

Fig S30. Fluorescence lifetime spectra of (A-C) photoluminescent particles and (D-F) three colored TBC samples. (G-I) Comparison of the fluorescence lifetime spectra of the particles and the TBC samples after normalization.

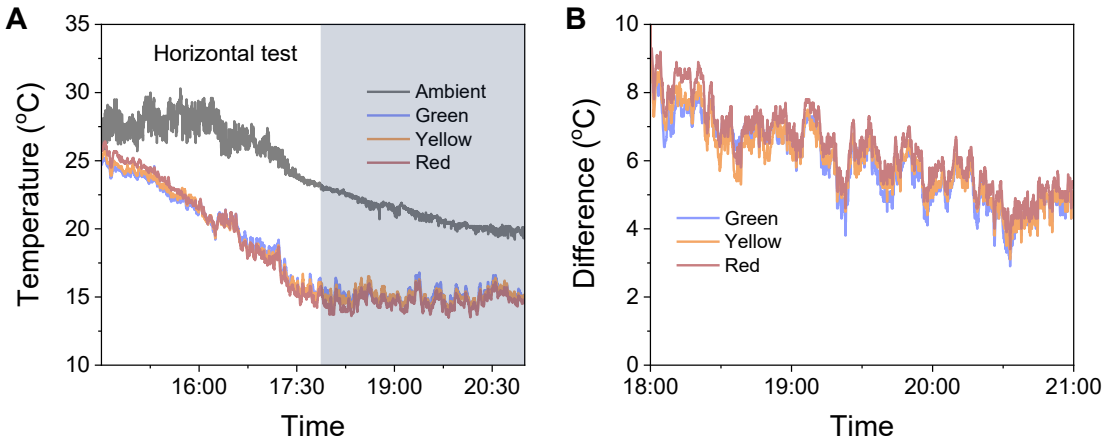

Fig S31. Real-time temperature curves (A) and their difference with ambient in temperature (B) of various TBC sample at night placed horizontally (Chengdu, October 23, 2024).

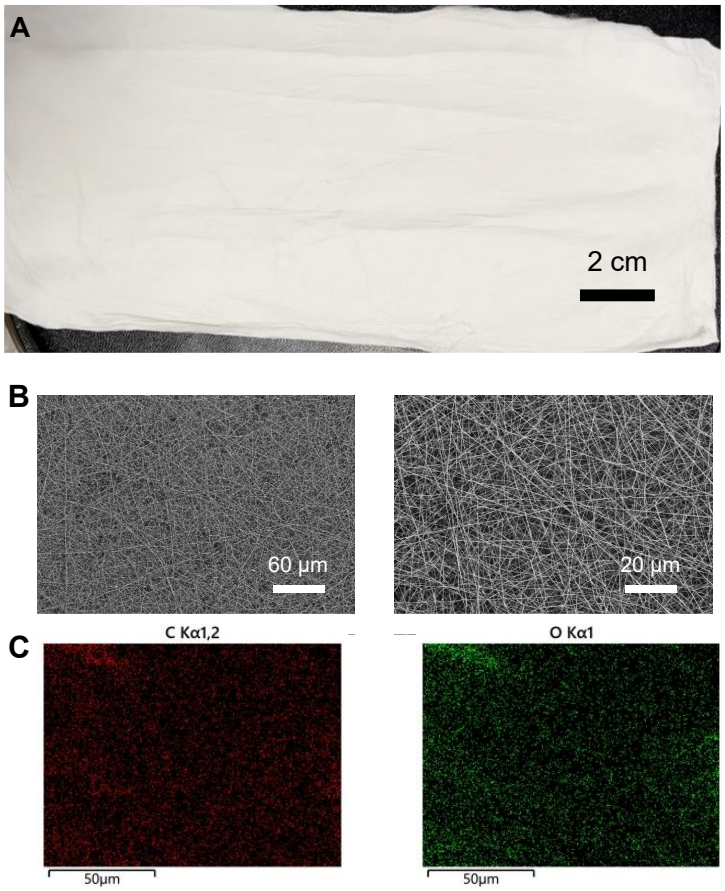

Fig S32. (A) Photograph of a selective sample prepared by electrostatic spinning, (B) SEM and (C) its elemental distribution.

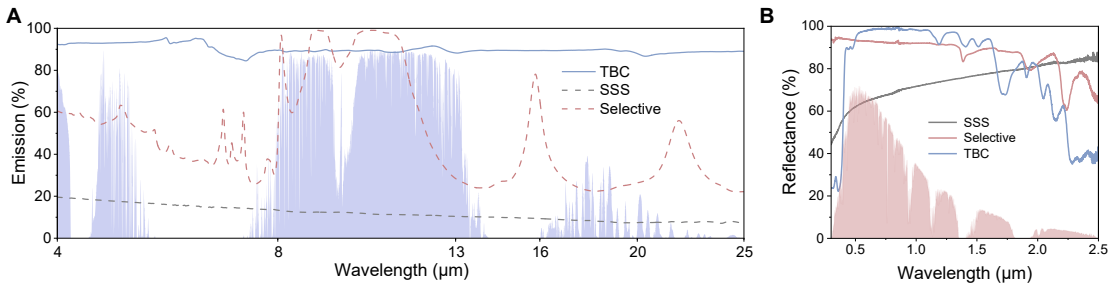

Fig S33. (A) Emissivity and (B) reflectance of a 200-μm-thick Selective sample, TBC and SSS.

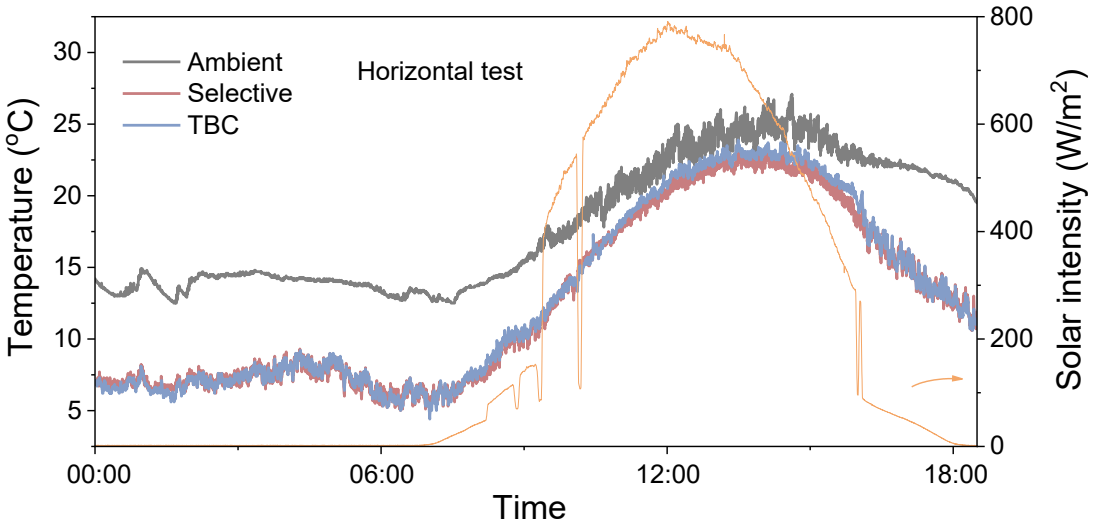

Fig S34. Real-time temperature curves of TBC and Selective sample when placed horizontally (Shenzhen, January 19, 2025).

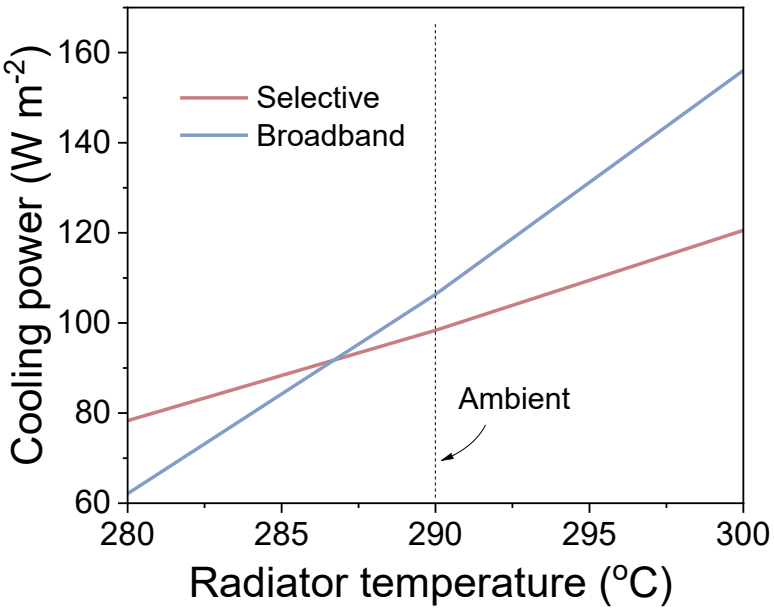

Fig S35. Net cooling power of selective and broadband coolers when placed horizontally at room temperature.

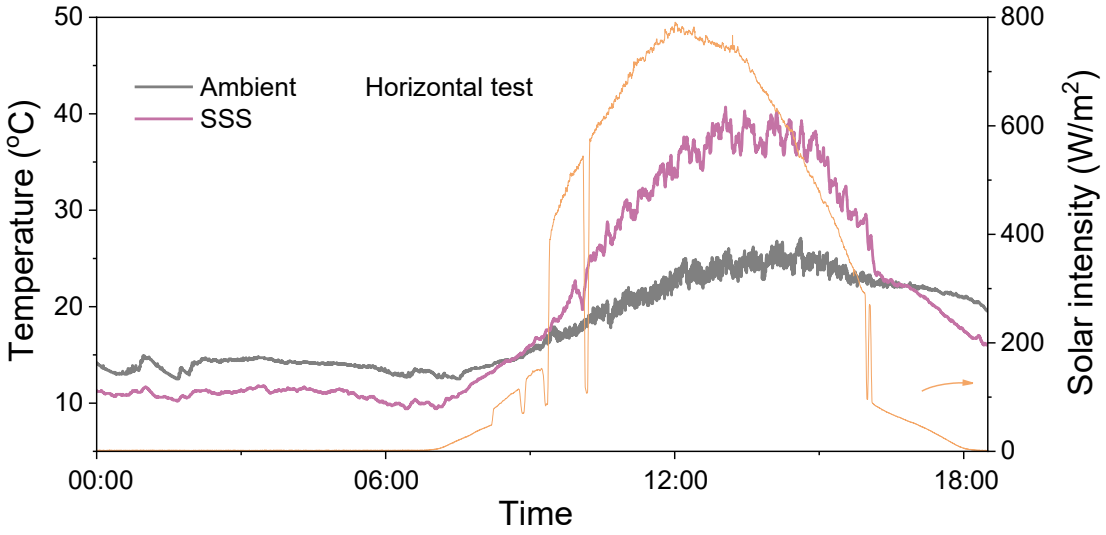

Fig S36. Real-time temperature curves of SSS sample when placed horizontally (Shenzhen, January 19, 2025).

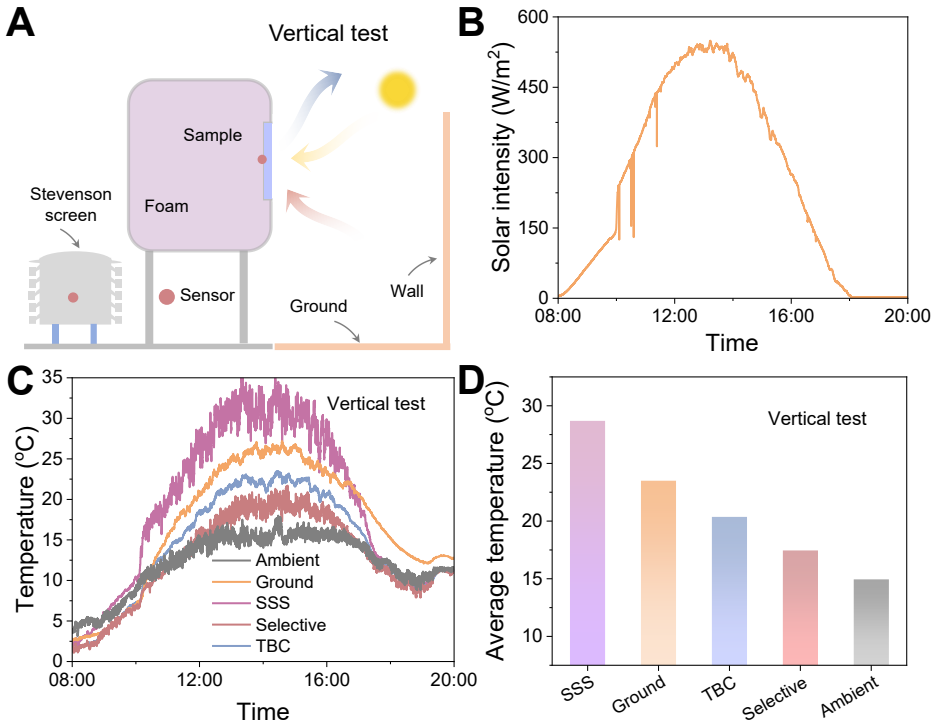

Fig S37. (A) Schematic of the device in the vertical direction at room temperature. (B) solar radiation intensity. (C) Real-time temperature curves of various sample when placed vertically (Chengdu, January 1, 2025). (D) Average temperature of various types of surfaces under direct sunlight (12:00-15:00) when placed vertically.

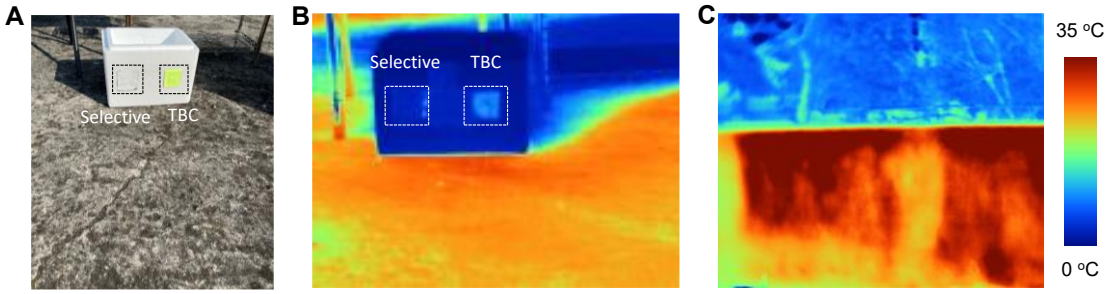

Fig S38. (A) Photographs of the samples during vertical testing. Infrared thermography of (B) samples and floors, and (C) walls during vertical testing.

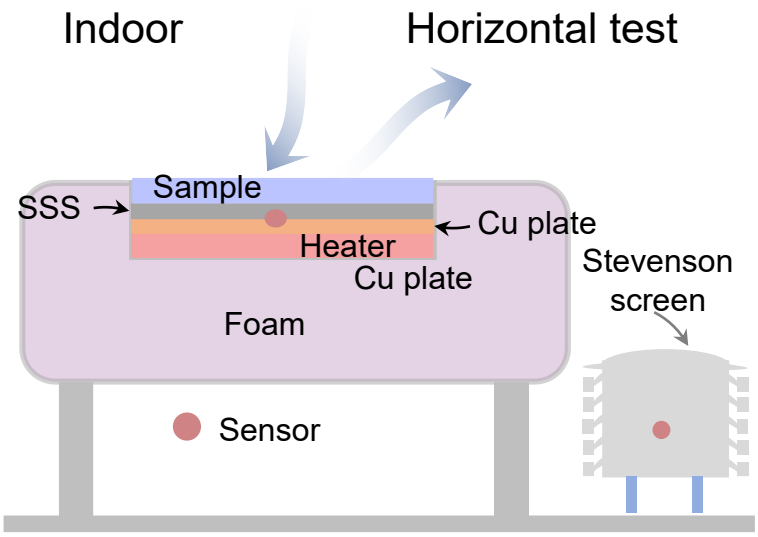

Fig S39. Schematic of the heat-load device placed horizontally in the room.

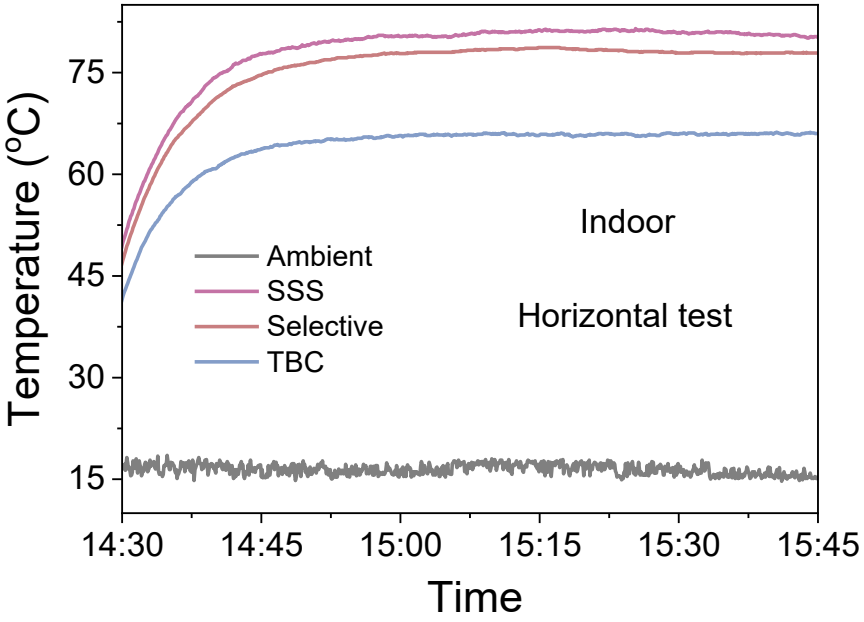

Fig S40. Real-time temperature curves of TBC, Selective, and SSS samples with a 600 W/m^2 heat load when placed horizontally in the room.

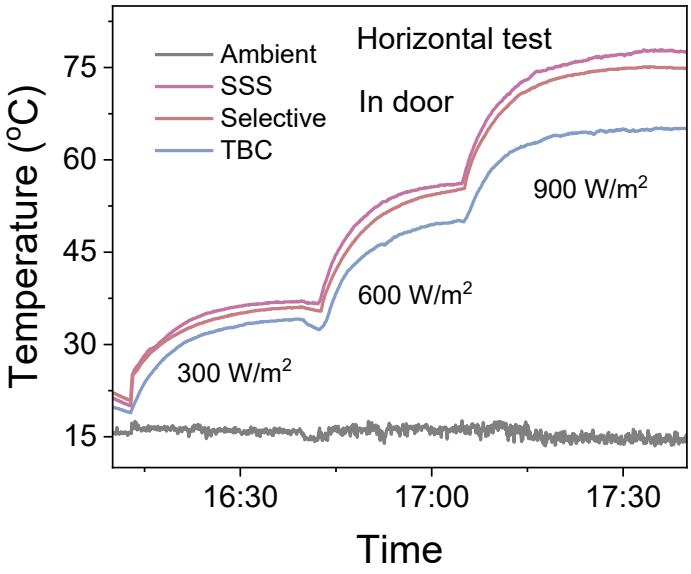

Fig S41. Real-time temperature curves of TBC, Selective and SSS sample when placed horizontally in the room.

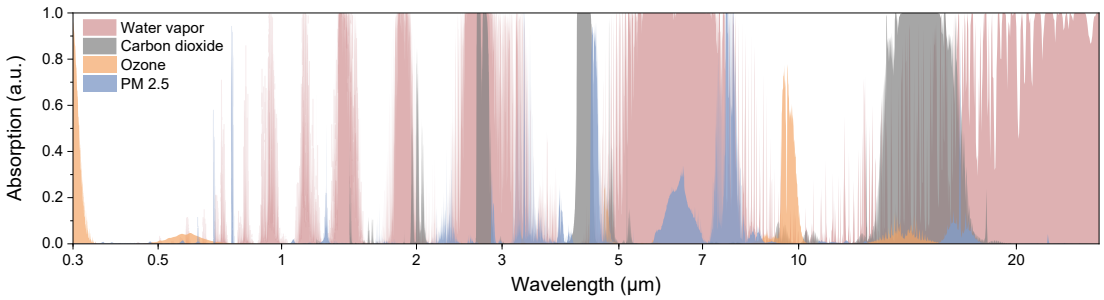

Fig S42. Absorption of several major atmospheric greenhouse gases in the mid-infrared region simulated by MODTRAN 5.0 software.

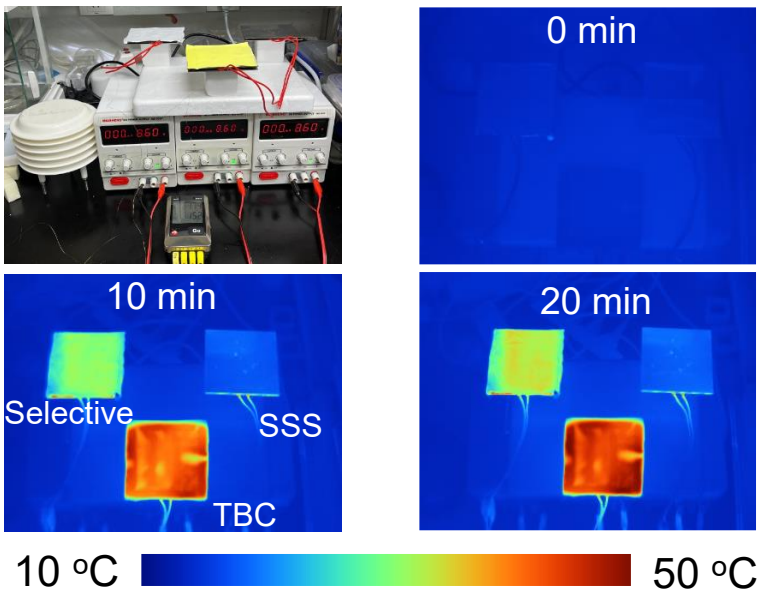

Fig S43. Real photos and their infrared thermography at different times for samples with a 600 W/m^2 heat load when placed horizontally in the room.

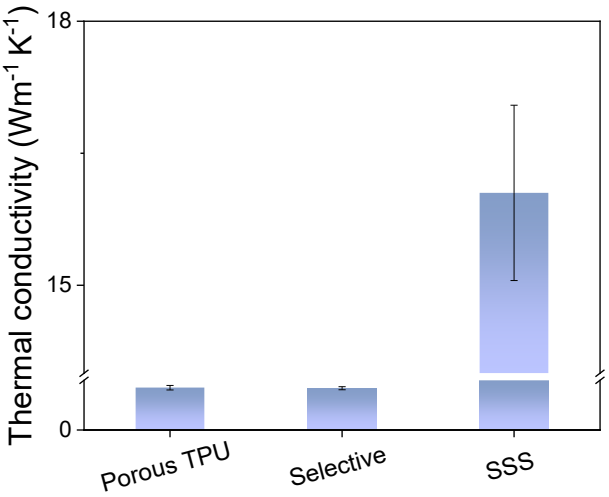

Fig S44. Thermal conductivity of porous TPU, Selective, and SSS.

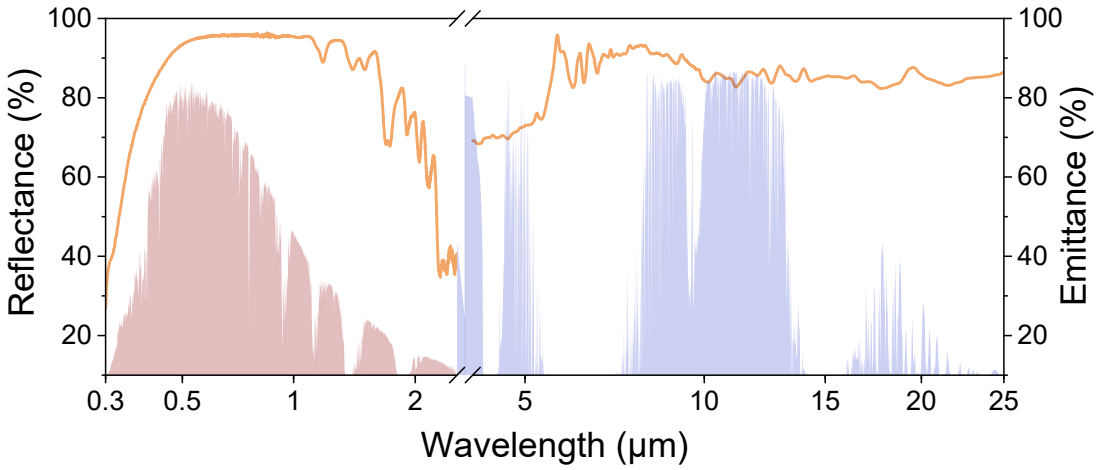

Fig S45. Reflectance and emissivity of a 200-μm-thick porous TPU.

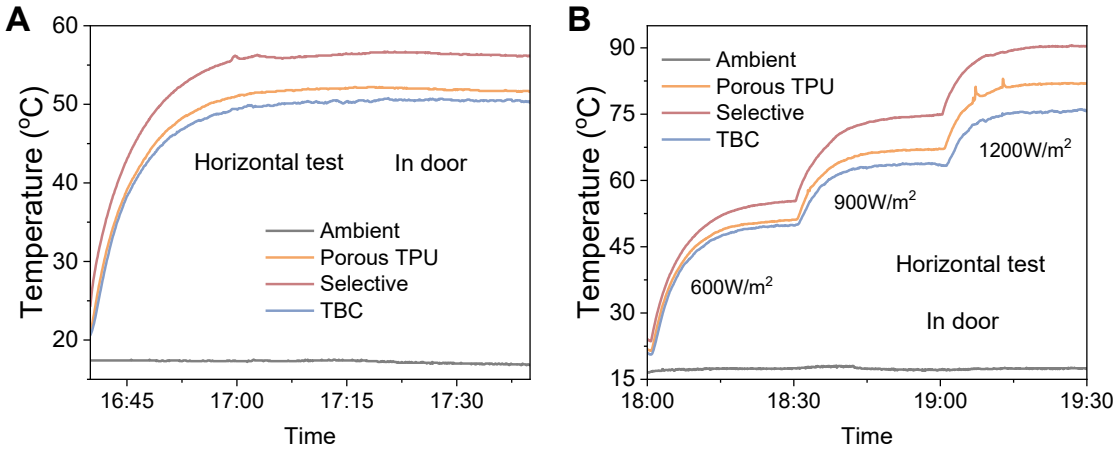

Fig S46. Real-time temperature curves of TBC, selective and porous TPU samples placed horizontally in the room, (A) with a heat load of 600 W/m^2, and (B) with different heat loads.

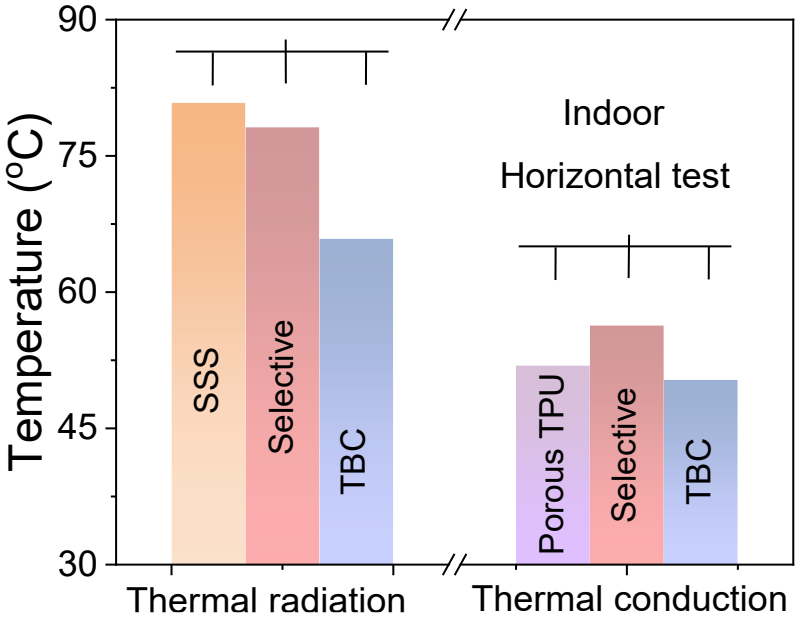

Fig S47. Average temperatures of various samples during horizontal indoor testing.

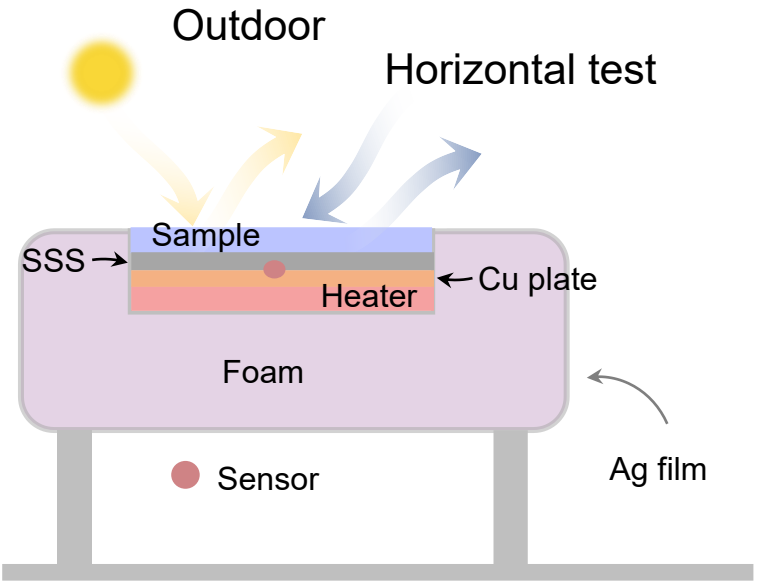

Fig S48. Schematic of the device with heat load when placed horizontally outdoors.

Fig S49. Photograph of an outdoor cooling test placed horizontally with a heat load of 600 W/m^2.

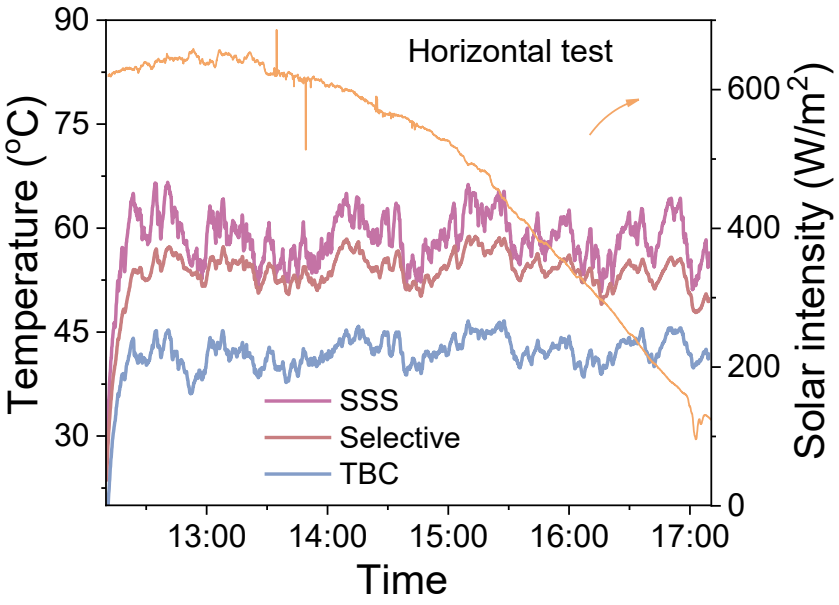

Fig S50. Real-time temperature curves of TBC, Selective, and SSS samples with a heat load of 600 W/m^2 when placed horizontally outdoors in direct sunlight (Chengdu, December 30, 2024).

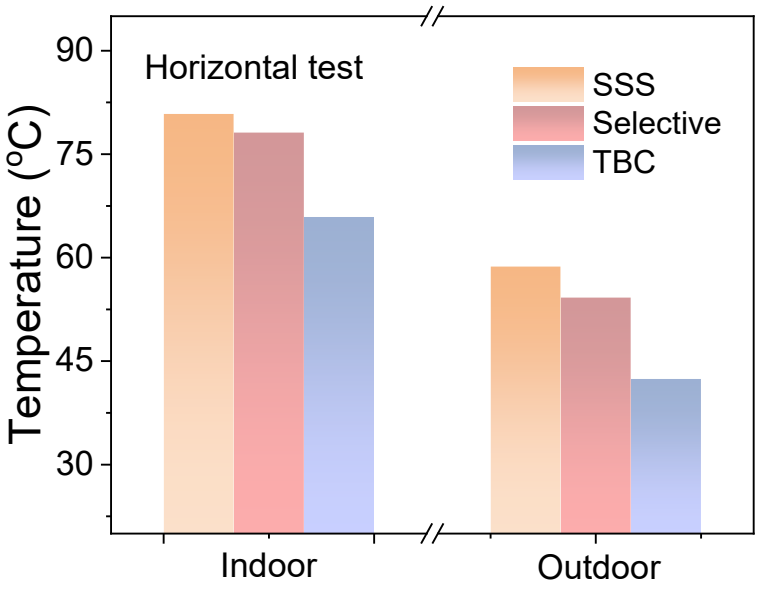

Fig S51. Average temperature of various samples during horizontal indoor and outdoor testing.

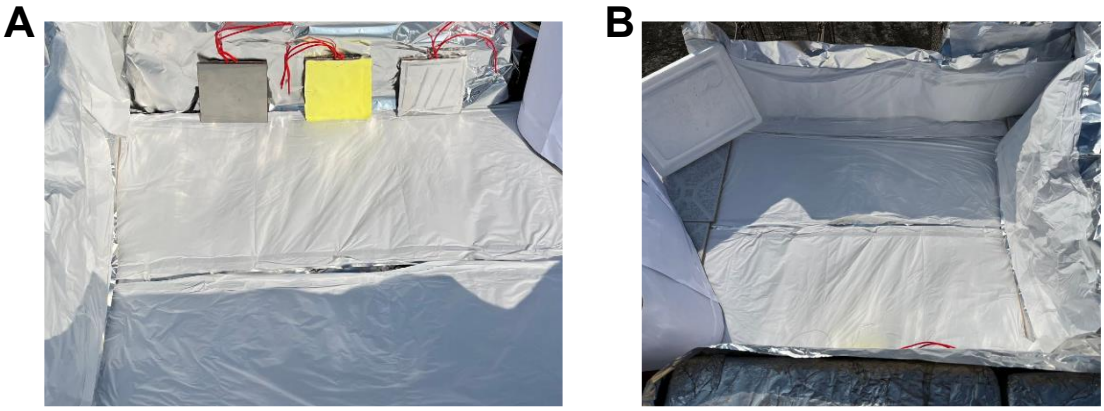

Fig S52. Photographs of TBC, selective, and SSS samples when placed vertically outdoors with a heating power of 600 W/m^2. To better highlight the performance differences between samples, a nanoparticle-filled PTFE film with high solar reflectance and high mid-infrared emissivity was used to simulate the cooler floor and wall surfaces, given that the device surface temperature significantly exceeds that of its surroundings.

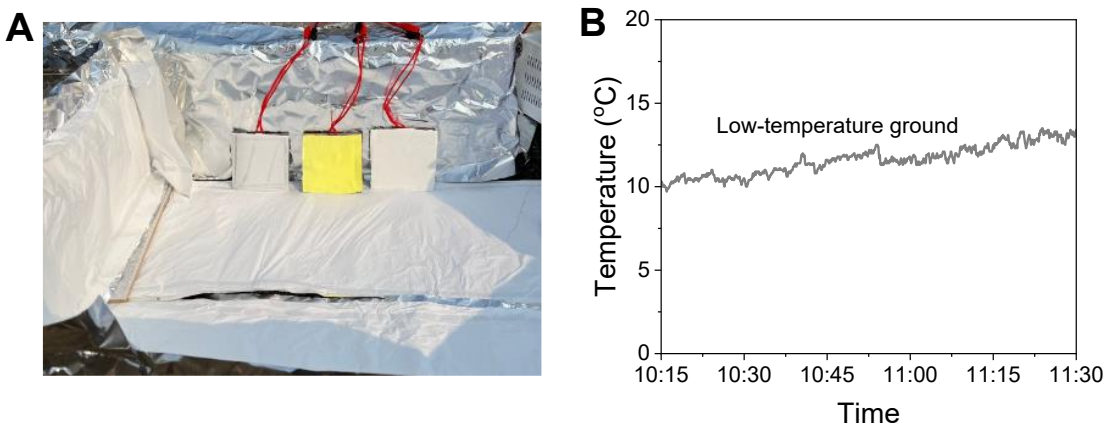

Fig S53. (A) Photographs of TBC, selective, and porous TPU samples when placed vertically outdoors with a heating power of 600 W/m^2. (B) Real-time temperature curves of the simulated ground.

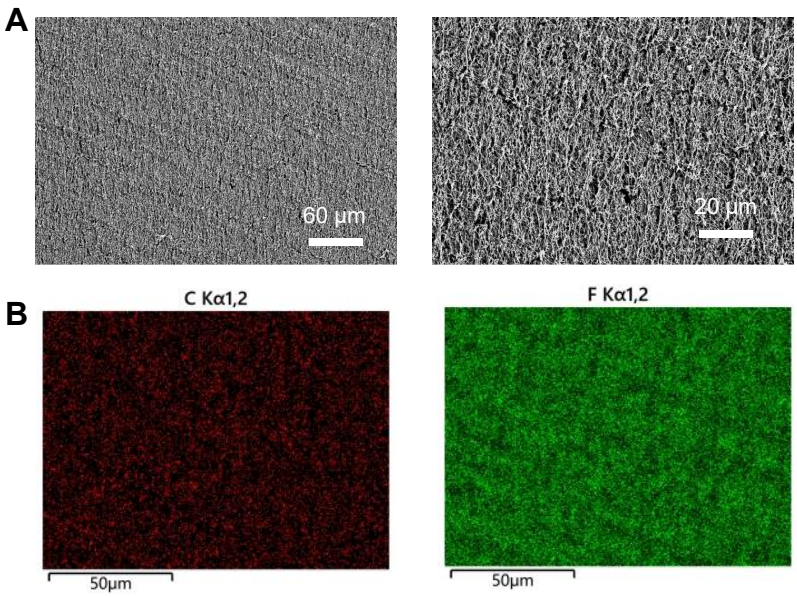

Fig S54. (A) SEM and (B) elemental distribution of nanoporous polytetrafluoroethylene films.

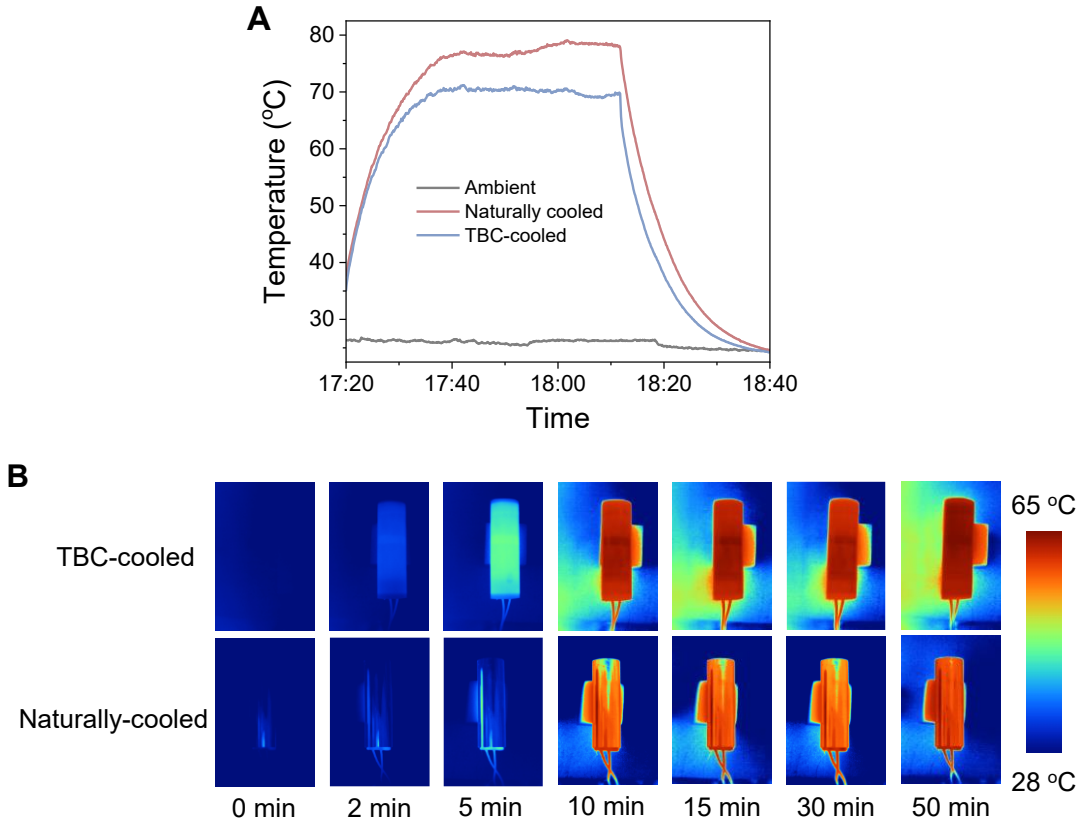

Fig S55. (A) Real-time temperature curves inside naturally cooled and TBC-cooled pipes (600W/m^2 heat load inside the pipe) in the room (Chengdu, September 5, 2024) and (B) their infrared thermal imaging.

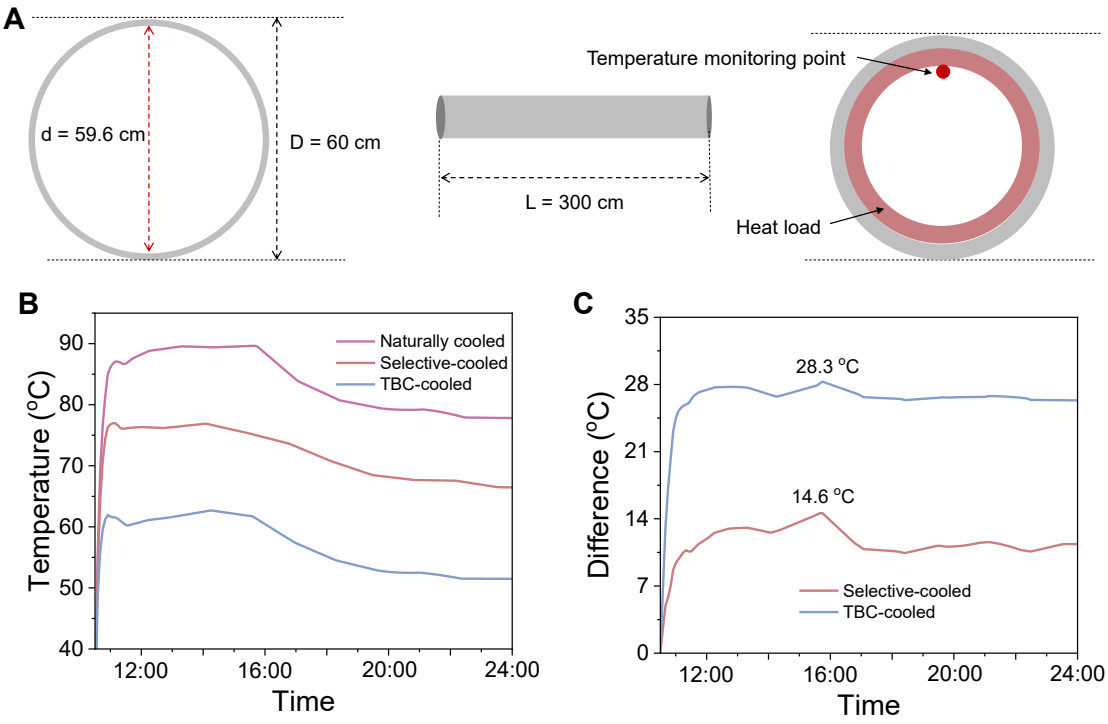

Fig S56. (A) Detailed parameters of the pipes model. Simulation results at a horizontal direction of pipe (B) inner surface temperature of various samples and (C) temperature difference with naturally cooled pipe (heating power 600 W/m^2).

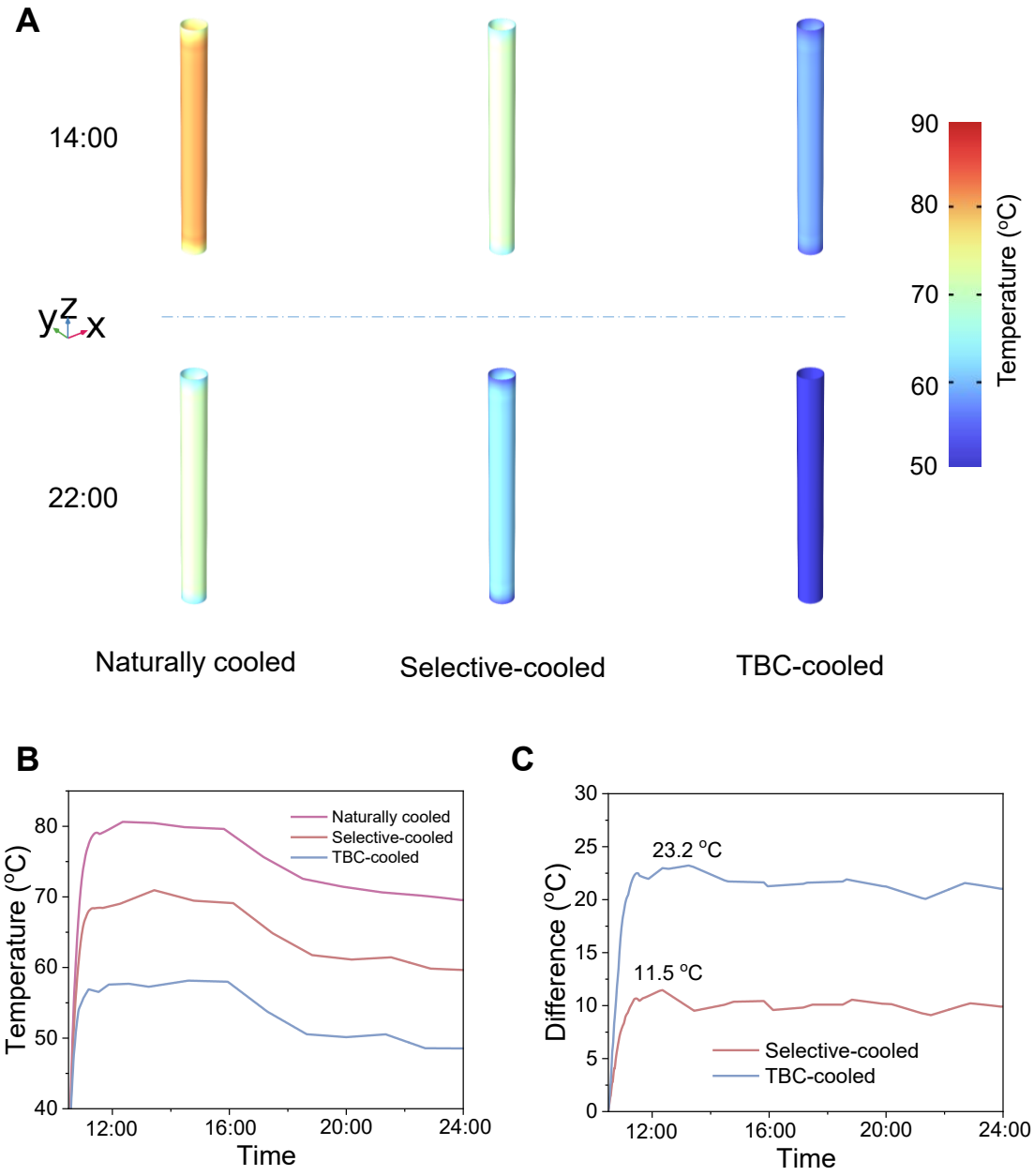

Fig S57. (A) Simulation results of internal temperatures of vertically placed pipes with a heating power 400 W/m^2, where x refers to North, y to West, and z to solar orientation. (B) inner surface temperature of various samples and (C) temperature difference with naturally cooled pipe (heating power 400 W/m^2).

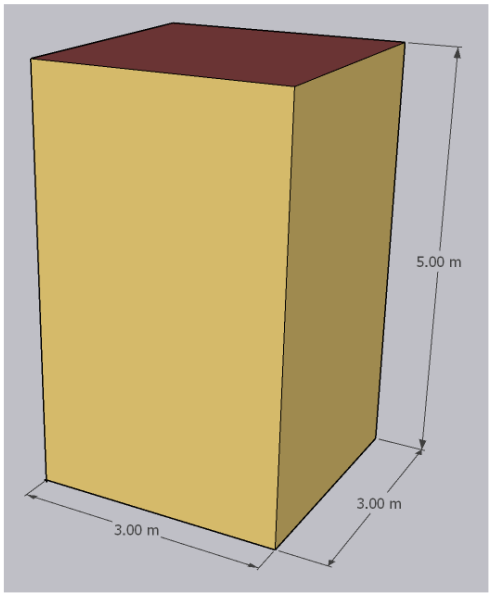

Fig S58. Three-dimensional view of the equipment room.

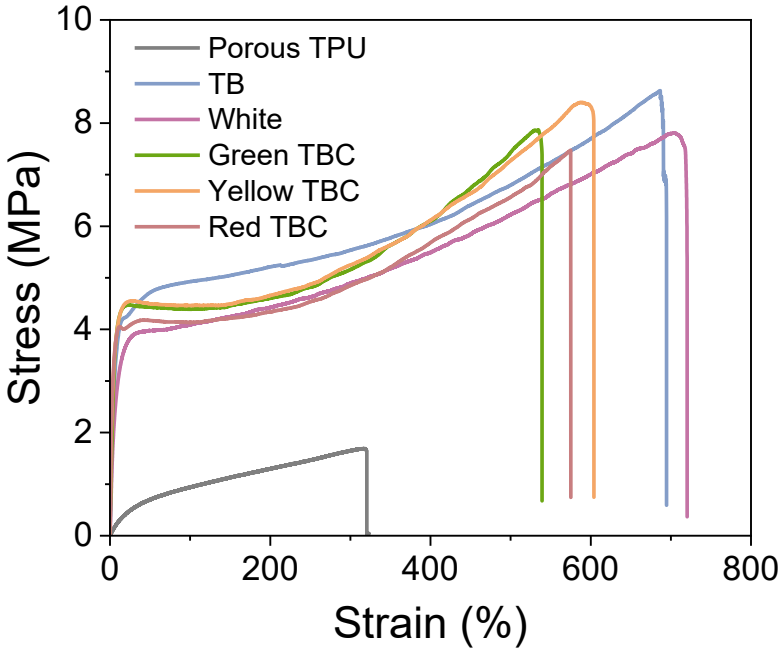

Fig S59. Tensile stress and strain of various samples.

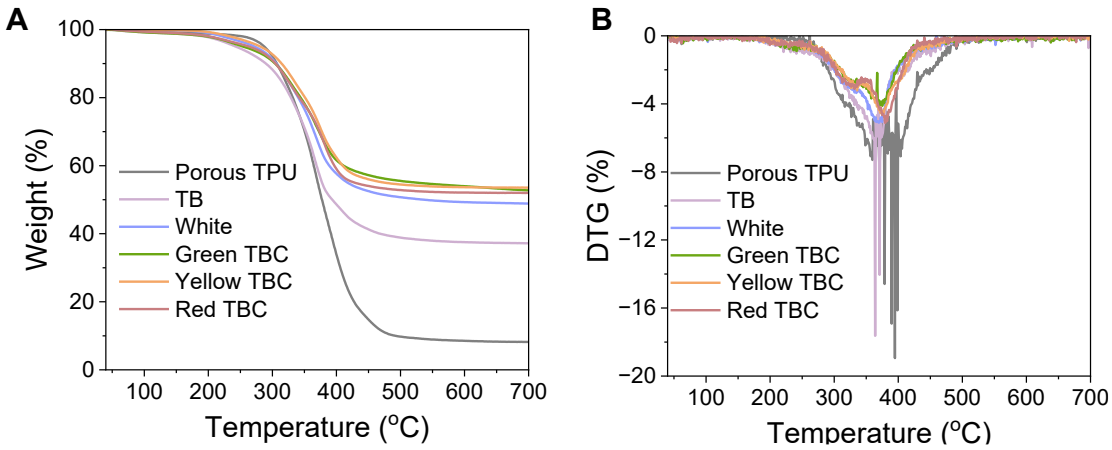

Fig S60. (A) Thermogravimetric and (B) thermal decomposition rates of various samples.

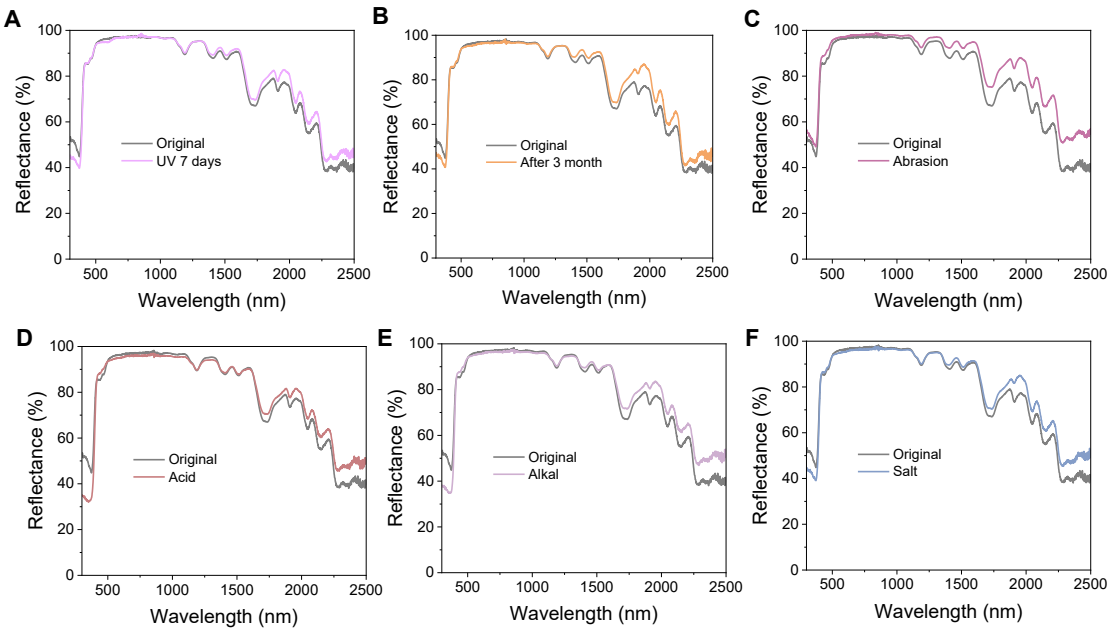

Fig S61. Solar reflectance of TBC samples (A) after 7 days of treatment with UV irradiation, (B) 3 months in air, (C) 1000 cycles of abrasion, and 7 days of treatment in (D) acid, (E) alkali, and (F) salt solutions, respectively.

Selective cooler	Broadband cooler
 People on the scorching ground	 Outdoor power lines and cables
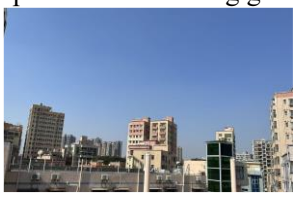 Urban complexes	 A cell tower on the green space
 Car on the scorching ground	 Equipment cabinet with a high proportion of greenery nearby
	 Equipment cabinets located near areas with a high concentration of greenery
	 Indoor heat-generating equipment

Table S1. Specific applications of Selective Coolers and Broadband Coolers. Common applications for selective coolers include fabrics, buildings, vehicles in urban areas, etc. Common applications for wide-band coolers including outdoor power lines, transformers, communication base stations, equipment enclosures, buildings with extensive greenery, indoor heat-generating equipments, etc.

	300 K	320 K	340 K	360 K	380 K	400 K
short-wave (2.5 - 8 μm)	19.01%	22.66%	26.36%	30.02%	33.63%	37.13%
long-wave (13 - 20 μm)	37.33%	33.81%	30.67%	27.88%	25.39%	23.17%

Table S2. Proportion of radiative energy emitted in the short-wave (2.5-8 μm) and long-wave (13-20 μm) infrared regions across different temperatures.

	1	2	3	average	error
porous TPU	0.07215	0.06511	0.06754	0.06827	0.00358
non-porous TPU	0.2273	0.2321	0.2281	0.22917	0.00257
TB film	0.7407	0.7514	0.7681	0.7534	0.01381

Table S3. Thermal conductivity of porous TPU, non-porous TPU, and TB film.

	White top	White cross	Green top	Green cross	Yellow top	Yellow cross	Red top	Red cross
Ti	0.5	0.27	/	/	/	/	/	/
Ba	/	/	0.62	0	/	/	/	/
Y	/	/			0.5	0	/	/
Sr	/	/	/	/	/	/	0.18	0.01

Table S4. Characteristic elements contents in the surface and cross-section of white film and various TBC films.

	Porous TPU	White film	SSS	Selective	TBC
8-13 μm (ATW)	87.60/87.37	88.21/87.49	11.72/11.76	77.42/78.50	90.06/89.95
2.5-25 μm	87.31/87.13	87.70/87.50	11.41/12.50	50.12/51.44	90.08/90.01
2.5-8 μm	87.61/85.26	87.04/88.23	15.02/15.51	39.95/42.53	90.12/91.4
13-25 μm	85.18/84.90	87.33/87.01	9.19/9.23	29.11/29.13	89.71/89.47
non-ATW	86.19/86.19	87.30/87.30	11.17/11.17	32.15/32.15	90.09/90.09
ATW/non-ATW	1.02/1.01	1.01/1.00	1.05/1.05	2.4/2.44	1.00/1.00

Table S5. Thermal emissivity (300/400 K) of various samples at various wavelengths in the mid-infrared.

Materials	Method	Thermal conductivity ($W\ m^{-1}\ K^{-1}$)	Cooling (below-ambient)	Cooling (above-ambient)	Color	Thickness (μm)	Ref
Coating	Layer-by-layer spraying	/	2.7 ℃	/	Yes	210	(45)
Film	Hot-pressing	1.3	4 ℃	18 ℃	No	1400	(47)
Coating	Layer-by-layer spraying	/	No	/	Yes	250	(48)
Film	Emulsion polymerization	0.58	7 ℃	15.3 ℃	No	2000	(49)
Film	Electrospinning	/	5.4-2.2 ℃	/	Yes	/	(11)
Fabric	Electrospinning	/	3.2 ℃	/	Yes	500	(50)
Film	Electrospinning	1	5.5	25.3℃	No	400	(12)
Film	Layer-by-layer self-assembly	8.9	/	17.8 ℃	Yes	96	(51)
Film	Vacuum filtration	1.77	/	2.5 ℃	No	/	(52)
Film	Self-stratification	0.753	3.4 ℃	27 ℃	Yes	200	Our work

Table S6. Comparison of TBC's overall performance with that of previous studies.

Reflectivity	Porous TPU	TB film	White film	SSS	Selective	TBC
0.3-2.5 μm	91.0	94.0	92.3	67.8	91.8	92.5

Table S7. Solar reflectivity of various samples at 0.3-2.5 μm. The reflectance of TBC refers to the effective reflectance with the addition of the photoluminescence effect.

	0 min	10 min	20 min
SSS	14 ℃	17.8 ℃	18.3 ℃
Selective	14.1 ℃	30.3 ℃	33.5 ℃
TBC	14.5 ℃	41.3 ℃	44.1 ℃

Table S8. Temperatures of SSS, Selective and TBC shown by the thermal imaging camera.

References and Notes

1. X. Wu *et al.*, A dual-selective thermal emitter with enhanced subambient radiative cooling performance. *Nat. Commun.* **15**, 815 (2024). 10.1038/s41467-024-45095-4
2. D. Li *et al.*, Scalable and hierarchically designed polymer film as a selective thermal emitter for high-performance all-day radiative cooling. *Nat. Nanotechnol.* **16**, 153-158 (2021). 10.1038/s41565-020-00800-4
3. A. P. Raman, M. A. Anoma, L. Zhu, E. Rephaeli, S. Fan, Passive radiative cooling below ambient air temperature under direct sunlight. *Nature* **515**, 540-544 (2014). 10.1038/nature13883
4. S. Fan, W. Li, Photonics and thermodynamics concepts in radiative cooling. *Nat. Photonics* **16**, 182-190 (2022). 10.1038/s41566-021-00921-9
5. R. Wu *et al.*, Spectrally engineered textile for radiative cooling against urban heat islands. *Science* **384**, 1203-1212 (2024). 10.1126/science.adl0653
6. F. P. Incropera, D. P. DeWitt, T. L. Bergman, A. S. Lavine, *vol. 6 of Fundamentals of Heat and Mass Transfer* (Wiley New York, ed. 6, 2006).
7. S. Kim, J. Shin, S. Kim, AT2ES: Simultaneous Atmospheric Transmittance-Temperature-Emissivity Separation Using Online Upper Midwave Infrared Hyperspectral Images. *Remote Sensing*. 2021 (10.3390/rs13071249).
8. X. Ma *et al.*, Effects of Stokes shift and Purcell enhancement on fluorescence-assisted radiative cooling. *Journal of Materials Chemistry A* **10**, 19635-19640 (2022). 10.1039/D2TA02259A
9. X. Ma *et al.*, Fluorescence-Enabled Colored Bilayer Subambient Radiative Cooling Coatings. *Adv. Opt. Mater.* **12**, 2303296 (2024). https://doi.org/10.1002/adom.202303296
10. R. Levinson, S. Chen, C. Ferrari, P. Berdahl, J. Slack, Methods and instrumentation to measure the effective solar reflectance of fluorescent cool surfaces. *Energy and Buildings* **152**, 752-765 (2017). https://doi.org/10.1016/j.enbuild.2016.11.007
11. X. Wang *et al.*, Sub-ambient full-color passive radiative cooling under sunlight based on efficient quantum-dot photoluminescence. *Science Bulletin* **67**, 1874-1881 (2022). https://doi.org/10.1016/j.scib.2022.08.028
12. X. Liu *et al.*, Hybrid Passive Cooling for Power Equipment Enabled by Metal-Organic Framework. *Adv. Mater.* **36**, 2409473 (2024). https://doi.org/10.1002/adma.202409473
13. Y. Xia *et al.*, Design and synthesis of novel microencapsulated phase change materials with enhancement of thermal conductivity and thermal stability: Self-assembled boron nitride into shell materials. *Colloids and Surfaces A: Physicochemical and Engineering Aspects* **586**, 124225 (2020). https://doi.org/10.1016/j.colsurfa.2019.124225
14. X. Meng *et al.*, Long alkyl chain-grafted carbon nanotube-decorated binary-core phase-change microcapsules for heat energy storage: Synthesis and thermal properties. *Solar Energy Materials and Solar Cells* **212**, 110589 (2020). https://doi.org/10.1016/j.solmat.2020.110589
15. R. Liu *et al.*, Materials in Radiative Cooling Technologies. *Adv. Mater.* **37**, 2401577 (2025). https://doi.org/10.1002/adma.202401577
16. Y. D. R. Machado, G. C. M. Germano, E. Pecoraro, A. M. L. M. Costa, I. C. S. Carvalho, Impact of SiO2 nanoparticle morphology on scattering efficiency for random lasers.

Optical Materials **148**, 114775 (2024). https://doi.org/10.1016/j.optmat.2023.114775
17. Y. Wang *et al.*, Anomalous thermal conductivity in 2D silica nanocages of immobilizing noble gas atom. *Applied Physics Letters* **124**, 122205 (2024). 10.1063/5.0200462
18. X. Yang, K. Y. Law, L. J. Brillson, Low energy cathodoluminescence spectroscopy of SiO2 nanoparticles. *Journal of Vacuum Science & Technology A* **15**, 880-884 (1997). 10.1116/1.580725
19. A. H. Aly *et al.*, Ultra-sensitive pressure sensing capabilities of defective one-dimensional photonic crystal. *Scientific Reports* **13**, 18876 (2023). 10.1038/s41598-023-45680-5
20. B. Dongre, J. Carrete, N. Mingo, G. K. H. Madsen, Ab initio lattice thermal conductivity of bulk and thin-film α-Al2O3. *MRS Communications* **8**, 1119-1123 (2018). 10.1557/mrc.2018.161
21. J. Wei *et al.*, Direct Measurement of Electronic Band Structures at Oxide Grain Boundaries. *Nano Letters* **20**, 2530-2536 (2020). 10.1021/acs.nanolett.9b05298
22. L. A. Mirza, R. O. Salih, N. R. Abdullah, Energetic stability, structural, electronic, and optical properties of CaCO3 polymorphs: A DFT study on calcite, aragonite, and vaterite using HSE06. *Solid State Communications* **404**, 116092 (2025). https://doi.org/10.1016/j.ssc.2025.116092
23. L. Momenzadeh *et al.*, The thermal conductivity decomposition of calcite calculated by molecular dynamics simulation. *Computational Materials Science* **141**, 170-179 (2018). https://doi.org/10.1016/j.commatsci.2017.09.033
24. https://refractiveindex.info/?shelf=main&book=BN&page=LeeNitride.
25. C. Maestre *et al.*, From the synthesis of hBN crystals to their use as nanosheets in van der Waals heterostructures. *2D Materials* **9**, 035008 (2022). 10.1088/2053-1583/ac6c31
26. S. Roy *et al.*, Structure, Properties and Applications of Two-Dimensional Hexagonal Boron Nitride. *Adv. Mater.* **33**, 2101589 (2021). https://doi.org/10.1002/adma.202101589
27. https://libeldoc.bsuir.by/handle/123456789/50134.
28. A. M. Alsaad *et al.*, Measurement and ab initio Investigation of Structural, Electronic, Optical, and Mechanical Properties of Sputtered Aluminum Nitride Thin Films. *Frontiers in Physics* **Volume 8 - 2020**, (2020). 10.3389/fphy.2020.00115
29. G. M. Prinz *et al.*, Photoluminescence, cathodoluminescence, and reflectance study of AlN layers and AlN single crystals. *Superlattices and Microstructures* **40**, 513-518 (2006). https://doi.org/10.1016/j.spmi.2006.10.001
30. S. Araki *et al.*, Fabrication of Zinc Oxide Nanopatterns by Quick Gel-Nanoimprint Process toward Optical Switching Devices. *Japanese Journal of Applied Physics* **52**, 03BA02 (2013). 10.7567/JJAP.52.03BA02
31. M. Choi *et al.*, High figure-of-merit for ZnO nanostructures by interfacing lowly-oxidized graphene quantum dots. *Nat. Commun.* **15**, 1996 (2024). 10.1038/s41467-024-46182-2
32. G. Endale, P. Loura, D. Mohan, Investigation of structural, morphological and nonlinear optical properties of ZnO thin films using reflective Z-scan technique. *Optical and Quantum Electronics* **55**, 1127 (2023). 10.1007/s11082-023-05431-2
33. S. L. Mikhailova *et al.*, Thermal Stability of the Structure and Optical Properties of Nanostructured TIO2 Films. *Russian Physics Journal* **63**, 2045-2051 (2021). 10.1007/s11182-021-02272-y
34. D. Music, B. Stelzer, Intrinsic Thermal Shock Behavior of Common Rutile Oxides. *Physics*.

2019 (10.3390/physics1020022).
35. M. O'Byrne *et al.*, Investigation of the anatase-to-rutile transition for TiO2 sol-gel coatings with refractive index up to 2.7. *Thin Solid Films* **790**, 140193 (2024). https://doi.org/10.1016/j.tsf.2023.140193
36. https://doi.org/10.48550/arXiv.1612.02627.
37. V. K. Ambasta, S. Ghosh, A. Sen, Exploring the electronic properties of doped zirconia for enhanced optoelectronic applications: A quantum chemical approach. *Journal of Physics and Chemistry of Solids* **197**, 112412 (2025). https://doi.org/10.1016/j.jpcs.2024.112412
38. Y.-b. Zhang, H.-z. Gu, L.-p. Fu, A. Huang, M.-j. Zhang, Fabrication and properties of lightweight zirconia with fine closed porosity. *Journal of Iron and Steel Research International* **31**, 1449-1458 (2024). 10.1007/s42243-023-01086-1
39. https://kaits.com.cn/Check.aspx?px=down&page=39.
40. https://coatings.sibelcotools.com/industrial-coatings/powder-coatings/baryte.
41. Z. Tong *et al.*, Electronic and phononic origins of BaSO4 as an ultra-efficient radiative cooling paint pigment. *Materials Today Physics* **24**, 100658 (2022). https://doi.org/10.1016/j.mtphys.2022.100658
42. https://tateho-chemical.com/products/tatecera-cmgh.
43. Y. Miao, H. Li, H. Wang, K. He, Q. Wang, First principles and Debye model study of the thermodynamic, electronic and optical properties of MgO under high-temperature and pressure. *International Journal of Modern Physics B* **32**, 1850047 (2017). 10.1142/S0217979218500479
44. L. Schifferle, S. Speziale, S. S. Lobanov, High-pressure evolution of the refractive index of MgO up to 140 GPa. *Journal of Applied Physics* **132**, 125903 (2022). 10.1063/5.0106626
45. J. Xu *et al.*, Colored radiative cooling coatings using phosphor dyes. *Materials Today Nano* **19**, 100239 (2022). https://doi.org/10.1016/j.mtnano.2022.100239
46. L. Zhu, A. Raman, S. Fan, Color-preserving daytime radiative cooling. *Applied Physics Letters* **103**, 223902 (2013). 10.1063/1.4835995
47. P. Li *et al.*, Thermo-Optically Designed Scalable Photonic Films with High Thermal Conductivity for Subambient and Above-Ambient Radiative Cooling. *Adv. Funct. Mater.* **32**, 2109542 (2022). https://doi.org/10.1002/adfm.202109542
48. Y. Chen *et al.*, Colored and paintable bilayer coatings with high solar-infrared reflectance for efficient cooling. *Sci. Adv.* **6**, eaaz5413 (2020). doi:10.1126/sciadv.aaz5413
49. W. Tang *et al.*, Cascaded Heteroporous Nanocomposites for Thermo-Adaptive Passive Radiation Cooling. *Adv. Mater.* **36**, 2310923 (2024). https://doi.org/10.1002/adma.202310923
50. X. Li *et al.*, Selective spectral absorption of nanofibers for color-preserving daytime radiative cooling. *Materials Horizons* **10**, 2487-2495 (2023). 10.1039/D3MH00391D
51. Y. Zhou, C. Lu, W. Wu, R. Xiong, Self-stratified photonic radiative cooling composites with asymmetric thermal conductivity. *Materials Horizons* **13**, 2989-3000 (2026). 10.1039/D5MH02199E
52. J. Xia *et al.*, High Thermal Conductivity and Radiative Cooling Designed Boron Nitride Nanosheets/Silk Fibroin Films for Personal Thermal Management. *ACS Applied Materials & Interfaces* **16**, 7732-7741 (2024). 10.1021/acsami.3c16602